Peer reviewed version

Link to published version (if available):

Link to publication record in Explore Bristol Research
PDF-document

University of Bristol - Explore Bristol Research
General rights

Magma Emplacement Rates and Porphyry Copper Deposits: Thermal Modeling of the Yerington Batholith, Nevada

Anne Schöpa,[1,2,†] Catherine Annen,[1] John H. Dilles,[3] R. Stephen J. Sparks,[1] and Jon D. Blundy[1]

[1] *School of Earth Sciences, University of Bristol, Wills Memorial Building, Bristol, United Kingdom BS8 1RJ*

[2] *German Research Centre for Geosciences GFZ, Telegrafenberg, Potsdam, Germany 14473*

[3] *College of Earth, Ocean, and Atmospheric Sciences, 104 CEOAS Admin Building, Oregon State University, Corvallis, Oregon 97331-5503, USA*

† Corresponding author: e-mail, schoepa@gfz-potsdam.de

Abstract

Many porphyry copper deposits are associated with granitoid plutons. Porphyry copper deposit genesis is commonly attributed to degassing of pluton-forming intermediate to silicic magma chambers during slow cooling and crystallization. We use numerical simulations of thermal evolution during pluton growth to investigate the links between pluton construction, magma accumulation and solidification, volatile release, and porphyry copper deposit formation. The Jurassic Yerington batholith, Nevada, serves as a case study because of its exceptional exposure, revealing the geometry of three main intrusions. The last intrusion, the Luhr Hill granite, is associated with economic porphyry copper deposits localized over cupolas where dikes and fluid flow were focused. Our simulations for the conceptual model linking porphyry copper deposits with the presence of large, highly molten magma chambers show that the Luhr Hill granite must have been emplaced at a vertical thickening rate of several cm/yr or more. This magma emplacement rate is much higher than the time-averaged formation rates of other batholiths reported in the literature. Such low rates, although common, do not lead to magma accumulation and might be one of the reasons why many granitoid plutons are barren. Based on our results, we formulate the new testable hypothesis of a link between porphyry copper deposit formation and the emplacement time scale of the associated magma intrusion.

Introduction

Many porphyry copper deposits are associated with granitoid plutons. Porphyry copper deposit genesis is attributed to the degassing of pluton-forming, intermediate to silicic magma chambers (e.g., Burnham, 1979; Dilles, 1987; Cloos, 2001; Sillitoe, 2010). These plutons are commonly envisioned as resulting from the slow cooling and crystallization of large magma chambers (e.g., Steinberger et al., 2013). However, most extant models of porphyry copper deposit genesis couple the formation of ore deposits and the cooling of a magma chamber but do not consider how, typically, hundreds of cubic kilometers of magma were emplaced into the upper crust. For example, several models assume an instantaneously emplaced, km-wide and km-thick source of heat (Cathles, 1977; Norton and Knight, 1977; Cathles et al., 1997; Steinberger et al., 2013). Such models implicitly assume that the processes of pluton growth are irrelevant to ore formation. However, high precision geochronological data (e.g., Coleman et al., 2004; Matzel et al., 2006; Michel et al., 2008) indicate that emplacement of many granitoid plutons is protracted. If we define magma as a silicate melt containing ≤50% crystals, then slow emplacement makes it implausible that a melt-dominated magma chamber with a volume similar to that of the final pluton volume ever existed (Glazner et al., 2004; Annen, 2009). Also, the protracted growth of a pluton involves simultaneous cooling and crystallization together with the release of volatiles that may contribute to ore formation. The volume of magma present during the growth of a pluton and the rate at which it crystallizes are constrained thermally by factors including the rate of magma emplacement, the emplacement temperature of the magma and its wall rocks, and the rate of heat loss to the surroundings by conduction and hydrothermal convection (Annen and Sparks, 2002; Annen et al., 2006, 2008; Michaut and Jaupart, 2006; Schöpa and Annen, 2013). These factors, in turn, are a function of intrusion geometry, emplacement style, and wall rock physical properties.

The recent literature on magmatic-hydrothermal mineral deposits suggests that volatile release and ore formation is of limited duration compared to the longer time scale of associated magmatism. At both Yanacocha, Peru, and El Teniente, Chile, for example, short duration ore-forming fluid flow events of <100,000 years are separated by gaps of 0.3 to 1 m.y. over a total period of magmatic activity of 2 to 6 m.y. (Longo et al., 2010; Spencer et al., 2015; Tapster et al., 2016). Time scales of 50,000 to 100,000 years for porphyry intrusions and mineralization are documented by U/Pb zircon ages at Bingham, Utah; Bajo de la Alumbrera, Argentina; Coroccohuayco, Peru (von Quadt et al., 2011; Chelle-Michou et al., 2015); and Don Manuel, central Chile (Gilmer et al., 2017).

As most felsic, pluton-forming magmas are volatile-bearing, volatile release plays

an important role in pluton evolution. Volatile separation from a magma is ultimately controlled by solubility, which in turn is a function of pressure and melt composition. Volatiles may separate from initially volatile-saturated magma as it ascends (decompresses) or from initially volatile-undersaturated magma as it crystallizes (first and second boiling, Burnham, 1979). Consequently, the temporal pattern of volatile release is expected to depend on pluton growth rate, crystallization history, and the volatile content of the emplaced magma.

In this paper, we use numerical simulations of thermal evolution due to pluton growth to investigate the links between pluton construction, magma accumulation, magma solidification, volatile release, and porphyry copper formation. The Jurassic Yerington batholith in western Nevada is used as a case study. The Yerington batholith is associated with economic porphyry copper deposits and is particularly suitable for modeling pluton growth because of exceptional exposure of an entire upper ~10-km-thick crustal section due to Basin and Range extensional tectonics that reveal the geometry of the intrusion (Proffett and Dilles, 1984). Detailed field mapping in combination with petrological and geochronological analyses have shed light on the emplacement style and duration of this composite pluton and its associated mineralization (Dilles, 1987). A thermal model can add information and place additional constraints on the interpretation of geology, geochronology, and petrology in relation to mineralization. The thermal models can estimate how magmas accumulate within the pluton, the rate at which magma intrusions crystallize, and how the rates of volatile release from magma develop over time. We note that Chelle-Michou et al. (2017) also investigated volatile release during and after pluton emplacement in the context of porphyry copper formation. We compare their results with ours.

Geologic Observations

Geologic setting

The Yerington batholith is a Middle Jurassic (169–168 Ma) composite silicic intrusive complex comprising about 250 km^2 of exposed plutonic rocks, which contains four discovered porphyry copper deposits (Fig. 1A; see table 1 of Dilles and Proffett, 1995, for Yerington metal resource estimates). Cenozoic Basin and Range normal faulting, extension, and related block rotation have revealed a vertical section through the batholith from about <1- to >6-km paleodepth (Dilles and Proffett, 1995), making the Yerington batholith a unique location to study intrusive relationships from batholith roof to floor (Fig. 1B). Field relations show that the batholith consists of three major, sequentially emplaced intrusions, which become richer in silica, smaller in volume, and more deeply emplaced over time. Intrusion started with emplacement of the McLeod Hill quartz monzodiorite, followed by the Bear quartz monzonite and finally the Luhr Hill granite (Fig. 1).

This last phase of intrusion includes granite porphyry dikes that are associated with copper mineralization. The dikes are linked to cupolas in the upper part of the Luhr Hill granite and intruded upward into older rocks (Fig. 1B) where they are associated with Cu-Fe sulfides and hydrothermal alteration (Dilles, 1987; Dilles and Einaudi, 1992). The numerical model described below is informed by these and the following observations and constraints.

Temporal constraints

Temporal constraints on the emplacement of the Yerington batholith are provided by U-Pb zircon geochronology. Using Thermal Ionization Mass Spectrometry (TIMS) methods, Dilles and Wright (1988) obtained ages of 169.4 ± 0.4 Ma (2σ errors) for the McLeod Hill intrusion and 168.5 ± 0.4 Ma for one of the youngest porphyry dikes, in agreement with SHRIMP $^{206}Pb/^{238}U$ ages (Dilles et al., 2015; Banik et al., 2017). A dacite lava of the Fulstone Spring volcanics, which demonstrably postdates the porphyry dikes of the Yerington batholith, has an age of 166.5 ± 0.4 Ma (Dilles and Wright, 1988). These data suggest about 0.9 ± 0.6 m.y. for emplacement and crystallization of the Yerington batholith.

Intrusion geometry and composition

Intrusion volumes estimated by Dilles (1987) are 1,000 km³ for the McLeod Hill quartz monzodiorite, 256 km³ for the Bear quartz monzonite, and 70 km³ for the Luhr Hill granite. The McLeod Hill intrusion is a high-K pyroxene-biotite and hornblende-biotite quartz monzodiorite (56–63 wt % SiO_2); the Bear intrusion is a hornblende (biotite) quartz monzonite (62–67 wt % SiO_2) with an upper border zone of granite (~69 wt % SiO_2), and the Luhr Hill intrusion consists of hornblende-biotite granite and granite porphyry dikes with identical mineralogy and composition (67–69 wt % SiO_2; Proffett and Dilles, 1984; Dilles, 1987). Detailed geologic mapping of exposures at Ann-Mason and Luhr Hill indicates that granite porphyry dikes can be traced downward into the Luhr Hill granite for up to 1 to 2 km and furthermore, that the grain size of the groundmass of the dikes increases downward from 0.02 mm to >0.2 mm until the dikes can no longer be distinguished from the host Luhr Hill granite (Proffett and Dilles, 1984; Dilles, 1984, 1987; Carten, 1986; Profett, 2009). On the basis of these gradational contacts and the identical mineralogy and compositions of the granite porphyry dikes and Luhr Hill granite, Dilles (1987) concluded that the dikes, extending over a vertical interval of >5 km (Fig. 1), were sourced from the upper and middle part of the Luhr Hill granite (cf. Burnham, 1979). Moreover, crosscutting relationships between different generations of dikes at both the Yerington Mine and Ann-Mason porphyry copper deposits indicate that the earliest dikes were sourced from the upper part of the Luhr Hill granite and later dikes from deeper positions, as much as 1.5 to 3 km below its roof.

There is compelling field evidence that the first intrusion of McLeod Hill quartz monzodiorite was episodically emplaced. There are numerous internal contacts of steeply dipping dikelike bodies 20 to 100 m in width in the Singatse and Wassuk ranges (Dilles, 1987; see map of Dilles, 1984; for location see stop 3 in fig. 1 of Dilles et al., 2000). A series of moderately to steeply dipping sills was emplaced into the north limb of an anticline (Proffett and Dilles, 1984; Einaudi, 2000). In contrast, both the Bear quartz monzonite and Luhr Hill granite lack internal contacts and are relatively homogeneous. These observations are consistent with efficient mixing of magmas and fast rates of emplacement, although slowly emplaced granitoids can also lack sharp contacts (Barboni et al., 2015).

Emplacement depths

The paleodepth of the top and bottom of each of the three main intrusive units at Yerington can be reconstructed from the depth in the crustal profile exposed by Basin and Range faulting (see table 1 of Dilles, 1987). For example, the McLeod Hill quartz monzodiorite intrudes cogenetic volcanics along a relatively horizontal but irregular roof at <1-km depth and is found in the deepest exposures at about 8-km depth. The Bear quartz monzonite has a nearly horizontal roof at approximately 2-km depth and extends to at least 7-km depth. In contrast, the roof of the Luhr Hill granite exhibits considerable relief and forms a series of cupolas as shallow as 2.5- to 5.5-km depth and also extends downward to a flat-bottomed base at 8-km depth (Dilles, 1987; Dilles and Proffett, 1995). Recent investigations of the cogenetic Artesia Lake volcanic section (Dilles and Wright, 1988; Lipske and Dilles, 2000) suggest it was uplifted and eroded slightly during the emplacement of the batholith prior to deposition of the Fulstone Spring volcanics, so depth estimates above may be increased by 0.5 to 1 km.

Water content

Depth of emplacement and mineral assemblages constrain water contents dissolved in the melt phase for the Yerington magmas to be at least 3 to 5 wt % (Dilles, 1987). The tops of the Yerington intrusions were emplaced at depths of 1 km (McLeod quartz monzodiorite), 2 km (Bear quartz monzonite), and 3 to 5 km (Luhr Hill granite), whereas the deepest exposures were emplaced at 8 km and imply water contents in the melt of 3 to 6 wt % if water saturated. Hornblende, which occurs in all three intrusions, requires 4 wt % or more water in the melt (Eggler, 1972; Naney, 1983; Loucks, 2014; Scaillet et al., 2016) and total pressure greater than 150 MPa (Scaillet et al., 2016) corresponding to ~5-km depth. Hornblende is a dominant and early ferromagnesian phase in the Bear quartz monzonite and Luhr Hill granite, supporting emplacement of water-saturated magmas. Augite, biotite, and FeTi oxides dominate the upper part of the McLeod Hill quartz monzodiorite and precede late hornblende in deep parts of the McLeod

Hill quartz monzodiorite. These observations can be explained either by emplacement of relatively higher temperature, water-saturated magma above the hornblende liquidus of ~950°C (Scaillet et al., 2016) or emplacement of initially water-undersaturated (<4 wt %) magma (Dilles, 1987). In the modeling below, we assume all magmas start with 6 wt % water dissolved in the melt phase, corresponding to a saturation pressure of 250 MPa (Newman and Lowenstern, 2002), so that they are water-saturated at all depths studied.

Other relevant observations

Contacts between intrusions are generally sharp, suggesting emplacement of the Bear quartz monzonite into fully crystallized parts of the McLeod Hill quartz monzodiorite and the Luhr Hill granite into fully crystallized parts of Bear quartz monzonite. The Luhr Hill granite has an upper contact that truncates steeply dipping internal intrusive contacts and magmatic foliations within the older McLeod Hill quartz monzodiorite (fig. 7 of Dilles et al., 2000; location is shown in their fig. 1, stop 3). Magmatic contacts and foliations in the McLeod Hill quartz monzodiorite are not deformed or deflected by intrusion of the Luhr Hill granite, suggesting that the McLeod Hill quartz monzodiorite below the irregular truncation surface has been removed by melting, partial melting, or stoping and subsidence. Early (pre-Luhr Hill) propylitic and calc-sodic veins in the McLeod Hill quartz monzodiorite, parallel to the porphyry dike swarm, imply that this intrusion deformed in a brittle way and had therefore cooled down significantly when the Luhr hill granite was emplaced (Dilles and Einaudi, 1992).

The granite porphyry dikes derived from the Luhr Hill granite contain 50 vol % phenocrysts of plagioclase, quartz, K-feldspar, hornblende, biotite, magnetite, and titanite. This assemblage suggests that these porphyritic dikes were emplaced at relatively low temperatures (~675°–700°C) and under water-saturated conditions (Dilles, 1987; Naney, 1983). This is consistent with the 650° to 700°C Ti-in-zircon temperature estimates from these dikes (Dilles et al., 2015) and with the near-solidus, water-saturated phase relationships of metaluminous silicic magmas at 100 to 300 MPa (Scaillet et al., 2016).

The zircons of the Luhr Hill granite and associated porphyries include a population (6/51 or ~12% of the total) that has similar trace element characteristics (on Eu/Eu* vs. Hf plots) to the zircons in the older Bear quartz monzonite and McLeod Hill quartz monzodiorite (Dilles et al., 2015). These zircons may have been recycled from these older intrusions into the younger Luhr Hill granite by mass transfer across the intrusive contacts, or they can result from source-region mixing of magmas prior to emplacement.

The roof of the Bear intrusion is characterized by leucocratic granite (Bear granite) about 100- to 200-m thick (~5 km^3) that grades downward into the main quartz

monzonite body and has been interpreted to result from filter pressing of silicic melts from quartz monzonite mush below (Dilles, 1987). The roof of the Luhr Hill intrusion lacks this voluminous silicic cap but is characterized by narrow aplite and pegmatite dikes, likely derived via filter pressing during crystallization of the Luhr Hill granite (Dilles et al., 2000).

Model Setup

Geometry

For our numerical model, the three intrusions of the Yerington batholith are assumed to have been emplaced successively (Fig. 2). We utilize an incremental model (Annen, 2009), in which an intrusion is emplaced at a constant rate. Such models of pluton growth are commonly described as "incremental," in which many successive small intrusive increments of fixed size are emplaced with a time interval between increments commensurate with the long-term average growth rate. Here, the discrete increments are no more than a computing convenience, and modeling results do not depend on the chosen size of each intrusive increment (Annen et al., 2008; Schöpa and Annen, 2013). This assumption is valid as long as the increments are small compared to the total and final size of the intrusion (for fuller discussions see Petford and Gallagher, 2001; Michaut and Jaupart, 2006; Annen, 2009). Thus, an incremental model may provide an accurate approximation for the case of continuous intrusion growth. Likewise, a model of incremental growth does not necessarily imply that the growth is episodic with fluctuations of emplacement rate or discrete pulses of emplacement. Thus, our modeling approach is valid even for the Bear quartz monzonite and the Luhr Hill granite where internal contacts are not observed in the field. In fact, a lack of internal contacts is common in intrusive bodies even where geochronological data or other structural evidence point to episodic emplacement (e.g., Glazner et al., 2004; Barboni et al., 2015). Additionally, internal contacts would not be evident where the magma chamber convectively mixes after emplacement.

For the sake of simplicity and to avoid mass balance issues, we model magma chamber growth as a series of discrete magma additions. Our model assumes that each intrusion has a fixed radius and grows by additions of horizontal increments so that the intrusion is a cylinder of fixed diameter that increases in thickness with time. Previous work has shown that the inclination of increments does not significantly affect the thermal evolution of a growing magmatic system (Annen et al., 2008). The top of each intrusion stays at a fixed depth below the Earth's surface, and the base moves downward as more magma increments are added. Our model contrasts with the model of Chelle-Michou et al. (2017), which keeps the intrusion depth constant, and the increments are cylinders emplaced at the center so that the intrusion diameter increases with time. Each disc-shaped magma

increment of our numerical model is 100 m thick. The choice of this thickness increment is justified by numerical efficiency. Results using smaller thicknesses are similar to those using 100 m (cf. Schöpa and Annen, 2013), but computing times are much longer. In fact, thermal evolution is controlled by the intrusion's average thickening or emplacement rate, i.e., by the increment thickness divided by the time interval between two increments, not by the volumetric emplacement rate (Petford and Gallagher, 2001; Michaut and Jaupart, 2006; Annen, 2009). The final height of the cylinder is 4 km for the McLeod Hill quartz monzodiorite and for the Bear quartz monzodiorite and 2 km for the Luhr Hill granite (Fig. 2A-D, Table 1). The lateral extensions of the three intrusions of the Yerington batholith are estimated from the geologic maps and associated cross sections (Proffett and Dilles, 1984; Dilles, 1987; Dilles and Proffett, 1995; Proffett, 2009). The modeled magma increments have a radius of 10 km for the McLeod Hill quartz monzodiorite and 4 km each for the Bear quartz monzonite and the Luhr Hill granite (Fig. 2A-D), corresponding to total intrusion volumes of 1,257, 201, and 100 km^3, respectively (Table 1). These volumes are within the errors of the geologic constraints and are similar to those from table 1 of Dilles (1987).

Based on field relationships described above, our model emplaces the first and topmost increment of the McLeod Hill quartz monzodiorite at a depth of 2 km, that of the Bear quartz monzonite at 3 km, and that of the Luhr Hill granite at 5.5 km (Fig. 2A-D, Table 1). The Bear quartz monzonite is emplaced into the lower part of the McLeod Hill quartz monzodiorite. For simplification of the model, we assume the Bear quartz monzonite displaces the McLeod Hill quartz monzodiorite downward to make space (Fig. 2). Similarly, the Luhr Hill granite is emplaced into the lower part of the Bear quartz monzodiorite, further displacing parts of the Bear quartz monzodiorite and the McLeod Hill quartz monzodiorite downward. This scheme of underaccretion is consistent with field observations demonstrating that the McConnell Canyon volcanics are found below the Yerington batholith at >7-km depth (Dilles and Wright, 1988). The Luhr Hill granite has an upper contact that clearly truncates steeply dipping contacts of the older intrusions. Some dikes can be traced downward at least 1 km into the upper parts of the Luhr Hill granite (Fig. 1B), with younger dikes traceable to greater depth, showing that the roof region had solidified while deeper parts of the pluton were still supplying magma into the dike system (Dilles, 1987). Later dikes can be traced to greater depths in the Luhr Hill granite, implying that magma was still present at depth when the roof region had solidified. Overaccretion, whereby successive magma increments intrude above precursor increments, could not generate these relationships. Similarly, the growth model of Chelle-Michou et al. (2017) does not reproduce these relationships, because in that case the cooled parts of the growing pluton are displaced outward. Other than by floor subsidence, some space of the intrusions is potentially accommodated by roof or wall-rock deformation (Morgan et al., 2008).

Heat computation

We have used field and geochronological criteria to constrain a sequence of intrusions as input to our thermal model (Fig. 2A-D). We numerically simulated the growth of the Yerington batholith with an explicit finite difference scheme where the temperatures, T, at each node of a numerical grid are obtained by solving the conductive heat flow equation

$$\frac{dT}{dt} = K\nabla^2 T - \frac{L}{c}\frac{\partial F}{\partial t} \qquad (1)$$

where ρ is the density (2,700 kg/m^3), c is the specific heat capacity (1,000 J/kg K), L is the latent heat of crystallization (3.5 × 10^5 J/kg), F is the melt (mass) fraction, and K is the thermal diffusivity (m^2/s) (Table 1). K is a temperature-dependent function as described in Whittington et al. (2009). The calculations are performed in cylindrical coordinates and the numerical domain is a 2-D slice of a 3-D system with the left side as the axis of symmetry (Fig. 2). The numerical domain represents the Earth's crust from the surface down to a depth of 15 km with a lateral extent of 15 km. A typical geothermal gradient of 30°C/km determines the initial temperatures at the nodes of the model before magma intrusion starts. The right side of the numerical domain is an insulating boundary, and the top (the Earth's surface) is at a constant temperature of 20°C.

Sensitivity analyses for these kinds of simulations showed that the main controlling parameter of a growing magma body thermal evolution is the emplacement rate. All other parameters, including conductivity, rock density, geothermal gradient, and temperature-melt fraction relationships, when varied within realistic ranges, are of second-order importance to the model results (Annen and Sparks, 2002; Annen et al., 2006, 2008; Michaut and Jaupart, 2006; Schöpa and Annen, 2013).

When a new magma increment is emplaced, the country rock or older intrusive units at the emplacement level are displaced downward while maintaining their physical characteristics, such as temperature and melt fraction. This resolution of the space problem via floor subsidence is strongly supported by the numerous observations of displaced wall rocks below many granitic plutons in general (e.g., Harrison et al., 1999; Michel et al., 2008) and the Yerington batholith in particular (Dilles and Wright, 1988; see above). The model does not consider magma transport through the crust, as we focus here on the large-scale thermal evolution of the intruded magma and its country rocks.

Temperature-melt fraction relationship

The crystallization of magma is described by the relationship between node temperature (T) and melt fraction (F). T-F relationships depend primarily on pressure and bulk composition, including H_2O contents (e.g., Scaillet et al., 2016). We matched the T-F relationships used in the model to the conditions and compositions of the three Yerington intrusions. On the basis of the mineral assemblages and Ti-in-zircon thermometers, we evaluated solidus temperatures of 680°C for the McLeod Hill quartz monzodiorite and the Bear quartz monzonite and 675°C for the Luhr Hill granite and liquidus temperatures of 970°C for the McLeod Hill quartz monzodiorite, 910°C for the Bear quartz monzonite, and 925°C for the Luhr Hill granite (Table 1). We approximated a T ($F = 0.6$) 800°C for the McLeod Hill quartz monzodiorite, T ($F = 0.5$) 750°C for the Bear quartz monzonite, and T ($F = 0.5$) 720°C for the Luhr Hill granite. The results are discrete T-F functions for each intrusion (Fig. 3).

Although the exact shape of the T-F functions affects the modeling results by less than 5%, it is worth noting that they are consistent with a diversity of published experimental phase relations for water-saturated silicic magmas of similar composition to those in the Yerington batholith (Fig. 3). The Tartara-San Pedro, Chile, dacite (Costa et al., 2004) is comparable to the composition of the McLeod Hill quartz monzodiorite, and the Wallowa, USA, granodiorite (Piwinskii and Wyllie, 1970) is comparable to the composition of the Bear quartz monzonite. For the Luhr Hill granite, we used a T-F relationship based on modeling work using MELTS (Bachmann et al., 2002; Huber et al., 2009) for appropriate granitic compositions. To avoid excessive numerical complexity, the T-F relations of the heating and cooling paths are identical. This can only happen if volatiles are available during remelting due to the strong effect of water content on melting relationships (Caricchi and Blundy, 2015). Because the cooling of hotter magma at the contact with the remelting material is required for this remelting to happen, our model implicitly assumes that volatiles are transferred simultaneously with heat within the magma. The transfer of volatiles away from the site of generation is a complex issue that is beyond the scope of this study, and we recognize this as a limitation of the model. Another limitation of the model is that we neglect the incorporation of volatiles by minerals.

Note also that we consider water to be the only magmatic volatile. Natural magmas contain CO_2, halogens, and sulfur species that also partition into the fluid phase, adding extra complexity. However, H_2O is by far the dominant volatile species in most silicic magmas, and we do not consider that the omission of other species will have significant effects on the thermal evolution modeled here, although the researcher should be aware of potential effects of other volatiles on phase relationships (e.g., melt fraction, mineral assemblage, fluid composition, etc.).

Calcic plagioclase (An_{55-85}), pyroxene, and local megacrysts of hornblende are found in the McLeod Hill quartz monzodiorite and other early units (fig. 12 of Dilles, 1987), suggesting that the Yerington magmas intruded with some suspended crystal loads. Therefore, the injection temperature of the magma increments of the McLeod Hill quartz monzodiorite was set to below the liquidus temperature at 920°C ($F = 0.9$). The Bear quartz monzonite and the Luhr Hill granite are characterized by relatively sodic plagioclase (An_{20-40}); the injection temperature for their magma increments was set to 850°C ($F = 0.8$ for the Bear quartz monzonite and $F = 0.9$ for the Luhr Hill granite; Table 1).

Magma convection

Internal intrusive contacts in the Bear quartz monzonite and the Luhr Hill granite have not been observed in the field and may have been erased by magma convection (Sparks et al., 1984; Dilles, 2000). In the numerical model, the effect of convection is approximated by homogenizing the temperature of connected nodes where the melt fraction is higher than 50%. This is an end member in terms of convection efficiency. Former sensitivity analysis (Annen et al., 2008) showed that the thermal evolution of a growing magma chamber that is modeled as fully conductive is similar to the thermal evolution of a magma chamber that is allowed to convect. This is due to the fact that the temperature gradient is almost flat in the fluid part of the chamber even in the conductive case. Most heat transfer occurs where the temperature gradient is steep, i.e., at the solid intrusion-country rock boundary.

At melt fractions lower than 50%, the system can be described as a magmatic mush. Viscosity increases greatly by a few orders of magnitude with small increases of crystal content in the transitional zone between magma (a suspension of crystals in melt) to mush (melt distributed within a touching framework of crystals). Whereas Rayleigh numbers typically exceed the critical value for convection in silicic magma layers more than a few meters thick (e.g., Couch et al., 2001), convection is suppressed in mush (Caricchi et al., 2007; Huber et al., 2010).

Volatile release

To investigate the relationship between magma intrusion and volatile release from the magma, we model the water content of the melt by assuming initial water saturation for all melts. In all the simulations, the melt is assumed to be water saturated and with an initial water content of 6 wt %. The mass fraction x of volatiles dissolved in the melt follows the solubility law

$$x = sP^n \qquad (2)$$

where s is the solubility coefficient, P is pressure, and n is a dimensionless exponent. For silicic magmas, $s = 4.11 \times 10^{-6}$ Pa$^{-1/2}$ and $n = 0.5$ (Sparks, 1978; Tait et al., 1989), which corresponds to a water content of 6 wt % at 8-km depth. In the pressure range of interest (30–150 MPa), this simple relationship reproduces the H_2O solubility model for rhyolites at 800°C of Newman and Lowenstern (2002) with an average absolute deviation of 0.14 wt % H_2O.

As the magma increments are emplaced, they cool, crystallize, and exsolve to release volatiles. We calculate how much water is dissolved in the melt of the magma increments during cooling at the respective emplacement depth for any time step of the simulations. We subtract this value from the total initial water content of the accumulated magma increments to calculate the amount of melt-derived water and use the injection interval to derive a volatile flux. Thus, we assume that all water is liberated from the growing intrusion efficiently and immediately as it separates from the melt.

Rate of magma emplacement and time scales

The emplacement of the Yerington batholith was simulated by emplacing each intrusion (McLeod Hill quartz monzodiorite, Bear quartz monzonite and Luhr Hill granite) at a steady rate with a repose period free of any magma injection between each of the intrusions. Different emplacement rates of magma injection (modeled with different time intervals between magma increment injections) and different repose times between the three main units of the Yerington batholith were investigated (Fig. 2E).

At the beginning of the simulations, each magma increment solidifies before the next one is emplaced. As the country rock heats up, at some time after the start of the simulation, one newly intruded magma increment will be emplaced when the previous increment is still partially molten. We call this time the "incubation time." For each of the three intrusive phases of the Yerington batholith, the incubation time is recorded. After intrusion growth ceases, the system cools down, and the time when there is no melt left is recorded. These two times divide the history of the magma system into three periods: (1) the incubation period of magma injection when no melt accumulates, (2) the magma accumulation period, and (3) the cooling and solidification period following emplacement of the final magma increment. We calculate volatile release patterns in each of these periods for the three intrusions of the batholith.

Hydrothermal convection

We do not model hydrothermal circulation in the country rocks. Thus, our model provides upper limits of cooling times and lower limits of intruding magma fluxes to build a large magma reservoir as first-order approximations of the thermal

evolution of the growing Yerington batholith. Hydrothermal convection of fluids through the hydrostatically pressured regime in the shallow crust above the magma chamber can significantly increase cooling rates of plutons (Cathles, 1977; Hayba and Ingbritsen, 1997). External hydrostatically advecting fluids are generally restricted to temperatures <400°C (e.g., Fournier, 1999; cf. Ingebritsen and Appold, 2012). In the Yerington district, externally convecting fluids contemporaneous with porphyry copper mineralization reach temperatures of up to 400° to 425°C (Carten, 1986; Dilles and Einaudi, 1992). Permeability decreases markedly with depth in the first few kilometers in the upper crust and for rocks at higher temperatures (Ingebritsen, 2012), so there will typically be a conductive zone between the top of a magma body and the region of hydrothermal convection. If this region is of the order of half to two-thirds of the depth from the surface to the top of the magma body, cooling could be increased by a factor of 2 or 3 at most, noting that there is also lateral heat loss. Thermal evolution is strongly controlled by magma flux, which is varied by factors of 10 in the simulations. Thus, we conclude that modification of the results of our model by hydrothermal cooling is of secondary importance and is addressed qualitatively in the discussion section.

Results

Intrusion scenarios with different emplacement rates of magma injection and different repose times between the three main intrusions of the Yerington batholith were designed (Fig. 2E). In all cases, the total time of emplacement does not exceed 1 m.y., consistent with geochronological data. We ran three simulations where each unit is emplaced at the same rate and the repose period between units is similar (Fig. 2E, scenarios I–III). To allow for an emplacement duration of 1 m.y. for the whole batholith, the emplacement rates are rapid when the repose periods are long and vice versa. We also ran two simulations where the emplacement rates of the three intrusions are different and increase from one intrusion to the next (Fig. 2E, scenarios IV, V).

Scenario I: Low emplacement rate; no repose period

One end member scenario is a continuous low emplacement rate of 1 cm/yr (volumetric emplacement rate is 3×10^{-3} km³/ yr for McLeod Hill quartz monzodiorite and 0.5×10^{-3} km³/yr for both Bear quartz monzonite and Luhr Hill granite, Table 2) with no repose period between the three intrusions (Fig. 2E, scenario I). Each magma increment completely solidifies before the emplacement of the next one. Thus, there is no long-term melt accumulation. At the end of each of the three intrusions, the temperature is everywhere below the solidus (Fig. 4). The results demonstrate that no magma chamber can form with low emplacement rates of 1 cm/yr.

Scenario II: Intermediate emplacement rate; intermediate repose periods

In this scenario, the emplacement rate is 2 cm/yr (volumetric emplacement rate is 6×10^{-3} km^3/yr for McLeod Hill quartz monzodiorite and 1×10^{-3} km^3/yr for both Bear quartz monzonite and Luhr Hill granite, Table 2). The repose period between McLeod Hill quartz monzodiorite and Bear quartz monzonite and between Bear quartz monzonite and Luhr Hill granite is 250 k.y. (Fig. 2E, scenario II). In this case, some melt accumulates (109 km^3 for the McLeod Hill intrusion and 11 km^3 for the Bear intrusion) but the melt fractions remain low (Fig. 5). The incubation periods, defined as the time span from the start of the magma emplacement to the point when permanent melt starts to accumulate, are 70 to 105 k.y. long and compose about half the total emplacement durations (Fig. 6, Table 2). Both McLeod Hill quartz monzodiorite and Bear quartz monzonite intrusions solidify during the repose periods prior to emplacement of the next intrusion. The maximum melt volume of the Luhr Hill granite (6 km^3) is only slightly higher than the volume of a single magma increment (Fig. 6). The emplacement of Bear quartz monzonite induces the remelting of 1.7 km^3 of McLeod Hill quartz monzodiorite, and the emplacement of Luhr Hill granite remelts 0.4 km^3 of Bear quartz monzonite, whereas the McLeod Hill quartz monzodiorite does not remelt.

Scenario III: Fast emplacement rate; long repose periods

In this scenario, the emplacement rate is 10 cm/yr for all three intrusions (volumetric emplacement rate is 31×10^{-3} km^3/yr for McLeod Hill quartz monzodiorite and 5×10^{-3} km^3/yr for both Bear quartz monzonite and Luhr Hill granite; Table 2), and the two repose periods are 450 k.y. (Fig. 2E). The high emplacement rate results in the fast accumulation of large volumes of magma with high melt fractions and in the development of transient substantial magma bodies with $F > 0.5$ (Fig. 7). The incubation periods are short, with time spans of less than 5 k.y. for each of the three intrusions (Fig. 6; Table 2). Large volumes of magma (600 km^3) with high melt fractions ($F > 0.6$) accumulate during the emplacement of McLeod Hill quartz monzodiorite (Fig. 6). Lower volumes (74 km^3) and slightly lower melt fractions ($F \sim 0.5$) characterize Bear quartz monzonite emplacement as the intrusion has a smaller total volume than the McLeod Hill quartz monzodiorite. Accumulated total melt volumes are even smaller for Luhr Hill granite (43 km^3), a result of the smaller intrusion dimensions with a thickness of 2 km compared to 4 km for the Bear and the McLeod Hill intrusions (Fig. 6). Magma crystallizes and solidifies completely for the McLeod Hill and Bear intrusions during the repose periods between the intrusions (Fig. 7). After intrusion emplacement has ceased, the McLeod Hill quartz monzodiorite solidifies in 174 k.y., the Bear quartz monzonite in 140 k.y., and the Luhr Hill granite in 63 k.y. The emplacement of the Bear quartz monzonite results in remelting of a small quantity of McLeod Hill quartz monzordiorite (1.2 km^3), and the emplacement of

Luhr Hill granite results in the remelting of 0.3 km^3 of Bear quartz monzonite but does not induce remelting of McLeod quartz monzodiorite.

Whatever the emplacement scenario, the remelting of McLeod Hill quartz monzodiorite by the Bear quartz monzonite and the remelting of Bear quartz monzonite by the Luhr Hill granite occur at the floor contact of Bear quartz monzonite and Luhr Hill granite, respectively. No remelting occurs at the roof contact. Volumes of melt in the earlier emplaced units are very small compared to the melt volumes accumulated in the actively emplaced unit (Fig. 6).

Scenarios IV and V: Increasing emplacement rates

The emplacement rates are 1 cm/yr (McLeod Hill quartz monzodiorite, volumetric emplacement rate 3 × 10^{-3} km^3/yr), 2 cm/yr (Bear quartz monzonite, volumetric emplacement rate 1 × 10^{-3} km^3/yr), and 10 cm/yr (Luhr Hill granite, volumetric emplacement rate 5 × 10^{-3} km^3/yr) for scenario IV and 4 cm/yr for scenario V (Luhr Hill granite, volumetric emplacement rate 2 × 10^{-3} km^3/yr), with repose periods of 100 k.y. and 250 k.y. (Fig. 2E, scenarios IV, V; Table 2). The results (Figs. 6, 8, 9) show no development of a magma chamber for the emplacement of McLeod Hill quartz monzodiorite but do show development of a magma chamber (with $F > 0.5$) for the Bear quartz monzonite (11 km^3). A large magma chamber develops for the Luhr Hill granite when emplaced at 10 cm/yr (43 km^3), and a smaller magma chamber forms (with $F > 0.5$) when the Luhr Hill granite is emplaced at 4 cm/yr (21 km^3). As in previous scenarios, the McLeod Hill quartz monzodiorite and Bear quartz monzonite have completely solidified by the time the Bear quartz monzonite and the Luhr Hill granite are emplaced.

Volatile (water) release

In our model, there are two contributions to volatile release. First, in all simulations the magmas are assumed to be initially water saturated with 6 wt %. As a consequence, some water is released simply due to decompression at the depth of increment emplacement. Second, following increment emplacement the saturated melts cool and crystallize, resulting in further volatile release. Cooling and crystallization occur for each magma increment. Here, we have added all these contributions together as our model is not attempting to model the details of volatile release over the short periods of the model time steps, noting again that the time steps are chosen for computing efficiency. Our aim is to model longterm variations of volatile (water) release.

At slow emplacement rate (scenario I), volatiles are continuously released throughout pluton emplacement. In all the scenarios (II-V) with higher emplacement rates, volatiles are released in three pulses, each associated with one of the three intrusions (Fig. 10). Each of these three pulses can be separated into

three stages of fluid release: an incubation stage prior to formation of a magma chamber, a magma chamber growth stage, and a postintrusion stage of cooling and crystallization following cessation of magma emplacement. The total volatile release naturally reflects the volume of each intrusion (Fig. 10). However, the larger intrusions (McLeod Hill quartz monzodiorite and Bear quartz monzonite) are not associated with mineralization, so here we focus on the results for the Luhr Hill granite (inset, Fig. 10). Here, the relationship between emplacement rate and timing of volatile release is evident. For a low emplacement rate of 2 cm/yr (scenario II), most of the volatile release occurs during the long incubation stage of >70 k.y. (Table 2) because no substantial magma chamber develops. In contrast, at higher emplacement rates of 4 cm/yr or more, significant amounts of volatiles are released during the magma chamber growth stage as a substantial magma chamber forms in only a few k.y. of incubation time (Table 2). The duration of the postintrusion volatile release stage increases with emplacement rate, as does the proportion of postintrusion volatile release, which accounts for 20% of the total volatile release for an emplacement rate of 4 cm/yr over 46 k.y. and for 40% for 10 cm/yr over 63 k.y. (Table 2). The remelting effect of earlier emplaced units on the volatile budget is negligible, as volatile masses from remelting are only up to 0.2% of the total volatiles released.

Volatile fluxes are low and at a constant rate for the three Yerington units for low magma emplacement rates (Fig. 11). Faster magma emplacement rates result in three volatile flux pulses, related to the emplacement of the three units. Absolute volatile flux peaks increase with higher emplacement rates (inset, Fig. 11). Constant volatile fluxes persist during incubation times when no melt accumulates. Peak volatile fluxes occur at the inception of magma chamber formation. After melt starts to accumulate, the volatile fluxes decline during the magma chamber growth stage and decline further after the end of magma emplacement during the postintrusion volatile release stage.

Discussion

Conceptual models of the relationship between porphyry copper deposits and associated granitoid bodies involve the presence of a large volume of magma and of a cupola that focuses the water-rich volatiles released by the subjacent magma. These features can be demonstrated from field geologic relationships at Yerington (Proffett and Dilles, 1984; Dilles, 1987; Proffett, 2009). In the Yerington case, we focus on the final Luhr Hill granite intrusion and seek to identify scenarios for generating a large volume of magma that can supply the hydrous fluids to form the porphyry copper deposits.

Geochronological studies typically yield long-term time-averaged rates of granitoid emplacement that are too low to form large magma chambers (de Saint-

Blanquat et al., 2011; Menand et al., 2015). Conductive thermal models indicate that magma flux rates of the order of 10^{-2} km^3/yr or more are needed (Annen 2009), noting that any additional cooling due to hydrothermal convection will require even higher rates for magma chamber formation. For the Yerington batholith, the geochronological data constrain the total emplacement duration of an estimated at least 1,560 km^3 of magma to about 1 m.y., giving an average volumetric emplacement rate of 1.5×10^{-3} km^3/yr. Even if the duration is minimized using the 2σ values of the zircon ages, the rate of 3×10^{-3} km^3/yr is still low. Thus, scenario I with continuous growth (1 cm/yr) and no gaps between the three constituent intrusions confirms that this scenario will not lead to magma chamber formation. We therefore conclude that the batholith was emplaced in pulses, separated by hiatuses (repose periods), consistent with the geologic field relationships of three successive plutons with clear crosscutting boundaries.

The simplest episodic model is for each pluton to be emplaced as a discrete entity with a constant emplacement rate and significant intervening repose periods. Scenario II (2 cm/yr horizontal emplacement rate) cannot reproduce a magma chamber for Luhr Hill granite with a volumetric emplacement rate of 10^{-3} km^3/yr. However, scenarios III and IV (10 cm/yr horizontal emplacement rate, equivalent to 5×10^{-3} km^3/yr for the Luhr Hill intrusion) generate a significant body of magma for the Luhr Hill granite. Scenario V requires rates of more than 4 cm/yr in order to generate a large magma body, thus high rates of Luhr Hill emplacement fit the conceptual model attributing porphyry copper deposit formation to the degassing and cooling of a substantial magmatic body. Increasing the rate to even higher values (25 cm/yr, results not shown) makes little difference in the results. All of the scenarios investigated indicate that the development of a magma chamber for Luhr Hill granite is only weakly dependent on the prewarming of the crust related to the previous McLeod and Bear intrusions. The modeled repose intervals are suitably long that the crust has cooled down significantly to nearly preintrusion, i.e., background, temperatures before the Luhr Hill granite is emplaced. This is consistent with field evidence of veins and hydrothermal alteration in the McLeod Hill quartz monzodiorite, suggesting that the older intrusions deformed in a brittle manner and thus had cooled sufficiently when the Luhr Hill granite was emplaced (Dilles and Einaudi, 1992). A shorter repose period between Bear quartz monzonite and Luhr Hill granite emplacement should enable Luhr Hill granite to form a magma chamber at slightly lower emplacement rates.

Our results show that the pattern of volatile release depends on emplacement rate (Figs. 10, 11). For low emplacement rates, no substantial magma body ever forms and volatile release takes place entirely during emplacement. Above a threshold of growth rate, a magma chamber can form and some volatiles are released postemplacement, during the period of magma chamber cooling and

crystallization. The higher the emplacement rate, the larger the contribution of postintrusive volatile release. Chelle-Michou et al. (2017) produced similar results (their fig. 4). Converting our results to km^3/yr to enable comparison, magma fluxes of 10^{-3} km^3/yr (2 cm/yr for Luhr Hill granite emplacement) show no postintrusion volatile release, in agreement with the results of Chelle-Michou et al. (2017) for the same flux. The postintrusion releases account for 20% of the total volatile release for 2×10^{-3} km^3/yr (4 cm/yr) and for 40% of the total for 5×10^{-3} km^3/yr (10 cm/yr) over tens of thousands of years. These results are in qualitative agreement with the results of Chelle-Michou et al. (2017) for rates of 10^{-2} and 10^{-1} km^3/yr. The comparison is limited by the fact that heat loss and thermal evolution of a cylinder that grows in thickness (our model) is different from the heat loss and thermal evolution of a cylinder that grows in radius (model of Chelle-Michou et al., 2017). Although we can only place lower constraints on the growth rate of the Luhr Hill granite at around 2×10^{-3} km^3/yr, there are empirical observations that are pertinent. Eruptive fluxes for continental volcanoes are typically between 10^{-3} and 10^{-2} km^3/yr (White et al., 2006), with more silicic magmas at the lower end and basalt volcanoes at the upper end of this range. We infer that growth rates of silicic intrusions are unlikely to greatly exceed 10^{-2} km^3/yr, in which case our thermal modeling results, supported by those of Chelle-Michou et al. (2017), indicate that postintrusion volatile release during cooling and crystallization of a magma chamber is important to consider.

If we assume 4 wt % of water in the melt instead of 6 wt %, the total water content would be 1.4×10^{14} kg and 36% lower than for 6 wt % H_2O. However, the general pattern of water release over time would not change for emplacement rates <4 cm/yr, because no large volumes of magma accumulate and volatiles are released during the incubation and the magma chamber growth stage. With 4 wt % volatile content, volatile saturation occurs at 3.5-km depth. With a high emplacement rate of 10 cm/yr, a higher fraction of volatiles (60% of the total volatile loss for the Luhr Hill granite, compared to 40% for 6 wt %) would be released during the postintrusion solidification stage. The fact that the top of the Luhr Hill granite lies at 2.5- to 5.5-km depth would be consistent with 4 wt % for stalling of magma ascent as a result of volatile loss.

One of the issues in understanding factors that lead to porphyry copper deposit formation is to explain associated barren intrusions. The Luhr Hill granite is associated with porphyry copper deposits, although it is the smallest of the three Yerington intrusions and therefore has the smallest volatile yield. One possible explanation for the difference is the formation of a Luhr Hill magma chamber, which requires a high emplacement (or vertical pluton thickening) rate. Although the volumetric emplacement rate might be small for the Luhr Hill granite compared to the McLeod Hill quartz monzodiorite and the Bear quartz monzonite at the same vertical thickening rate, the volume is emplaced into a rather small

plan area, and that results in a large magma chamber. In the case of slow emplacement rates, although volatiles are generated, they are not stored because a large volume of melt is never generated. The volatiles are released slowly, and volatile fluxes are low (Fig. 11). In the model, volatile fluxes are highest at high emplacement rates and during the incubation period and early stages of magma chamber formation (Fig. 11).

Another factor here might be that ore formation requires focused flow. In the case of McLeod Hill quartz monzodiorite and Bear quartz monzonites, the volatiles might have been released over the entire upper surface of the intrusion (cf. Dilles, 1987) rather than via a cupola or other focusing pathway. The combination of unfocused flow and low volatile fluxes may not enable conditions for orebody formation, and at Yerington they did not produce porphyry Cu ores above the Bear intrusion (Dilles, 1987). In contrast, our thermal model supports rapid emplacement of the Luhr Hill granite in order to form a magma chamber. This chamber was also the source of porphyry dike swarms emplaced through cupolas on the roof that are closely associated with porphyry copper deposit (Fig. 12). These circumstances suggest high volatile fluxes during and after intrusion emplacement, with repeated breaking of the intrusion roof to form tens of dikes in swarms and providing high permeable pathways for fluid escape (see Proffett, 2009). Thus, focused flow paths and high volatile fluxes provide conditions favorable for ore formation.

Conclusion

Our numerical simulations show that to comply with the conceptual model linking porphyry copper deposits with the presence of large, highly molten magma chambers, magmas must be emplaced at a high rate of several cm/yr (>2 × 10^{-3} km^3/yr). In plutonic records, such high rates are uncommon. It follows that either the current conceptual model is incorrect or that porphyry copper deposits are only produced by the episodically and rapidly emplaced plutons. The fact that many granitoid plutons are barren might be because they emplaced too slowly. Such granitoids do not accumulate melts, release volatiles early during emplacement, and are unlikely to form cupolas that channel the volatiles. In the case of the Yerington batholith, the formation of a magma chamber requires a magma emplacement rate higher than 4 cm/yr (equivalent to 2 × 10^{-3} km^3/yr) and repose periods between each of the three units exceeding 100 k.y. Since only the last emplaced unit (Luhr Hill granite) is associated with porphyry copper deposits, we suggest that this fertile unit might have been emplaced more rapidly (larger accumulation rate of magma within a magma chamber of small area) than its predecessors. New detailed, high-precision geochronological data are needed to test this hypothesis. Field relationships suggest that the porphyry copper dikes are emplaced during magma chamber growth, which is the period of peak volatile

fluxes in our numerical simulations. Thus, we infer from the numerical model that dike emplacement and high volatile flux are linked to magma chamber formation.

Acknowledgments

REFERENCES

Annen, C., 2009, From plutons to magma chambers: Thermal constraints on the accumulation of eruptible silicic magma in the upper crust: Earth and Planetary Science Letters, v. 284, p. 409–416.

Annen, C., and Sparks, R.S.J., 2002, Effects of repetitive emplacement of basaltic intrusions on thermal evolution and melt generation in the deep crust: Earth and Planetary Science Letters, v. 203, p. 937–955.

Annen, C., Scaillet, B., and Sparks, R.S.J., 2006, Thermal constraints on the emplacement rate of a large intrusive complex: The Manaslu Leucogranite, Nepal Himalaya: Journal of Petrology, v. 47, p. 71–95.

Annen, C., Pichavant, M., Bachmann, O., and Burgisser, A., 2008, Conditions for the growth of a long-lived shallow crustal magma chamber below Mount Pelee volcano (Martinique, Lesser Antilles Arc): Journal of Geophysical Research, v. 113, doi:10.1029/2007JB005049.

Bachmann, O., Dungan, M.A., and Lipman, P.W., 2002, The Fish Canyon magma body, San Juan volcanic field, Colorado: Rejuvenation and eruption of an upper crustal batholith: Journal of Petrolology, v. 43, p. 1469–1503.

Banik, T.J., Coble, M.A., and Miller, C.F., 2017, Porphyry Cu formation in the middle Jurassic Yerington batholith, Nevada, USA: Constraints from laser Raman, trace element, U-Pb age, and oxygen isotope analyses of zircon: Geosphere, v. 13, doi:10.1130/GES01351.1.

Barboni, M., Annen, C., and Schoene, B., 2015, Evaluating the construction and evolution of upper crustal magma reservoirs with coupled U/Pb zircon geochronology and thermal modeling: A case study from the Mt. Capanne pluton (Elba, Italy): Earth and Planetary Science Letters, v. 432, p. 436–448.

Burnham, C.W., 1979, Magmas and hydrothermal fluids, *in* Barnes, H.L., ed., Geochemistry of hydrothermal ore deposits, 2nd ed.: New York, Wiley, p. 71–136.

Caricchi, L., and Blundy, J., 2015, Experimental petrology of monotonous intermediate magmas: Geological Society, London, Special Publications, v. 422, p. 105–130.

Caricchi, L., Burlini, L., Ulmer, P., Gerya, T., Vassalli, M., and Papale, P., 2007, Non-Newtonian rheology of crystal-bearing magmas and implications for magma ascent dynamics: Earth Planet Science Letters, v. 264, p. 402–419.

Carten, R.B., 1986, Sodium-calcium metasomatism: Chemical, temporal, and spatial relationships at the Yerington, Nevada, porphyry copper deposit: Economic Geology, v. 81, p. 1495–1519.

Cathles, L.M., 1977, An analysis of the cooling of intrusives by ground-water convection which includes boiling: Economic Geology, v. 72, p. 804–826.

Cathles, L.M., Erendi, A.H.J., and Barrie, T., 1997, How long can a hydrothermal system be sustained by a single intrusive event?: Economic Geology, v. 92, p. 766–771.

Chelle-Michou, C., Chiaradia, M., Selby, D., Ovtcharova, M., and Spikings, R.A., 2015, High-resolution geochronology of the Coroccohuayco porphyry-skarn deposit, Peru: A rapid product of the Incaic orogeny: Economic Geology, v. 110, p. 423–443.

Chelle-Michou, C., Rottier B., Carrichi, L., and Simpson, G., 2017, Tempo of magma degassing and the genesis of porphyry copper deposits: Nature Scientific Reports, v. 7, doi: 10.1038/srep40566.

Cloos, M., 2001, Bubbling magma chambers, cupolas, and porphyry copper deposits: International Geology Review, v. 43, p. 285–311.

Coleman, D.S., Gray, W., and Glazner, A.F., 2004, Rethinking the emplacement and evolution of zoned plutons: Geochronologic evidence for incremental assembly of the Tuolumne intrusive suite, California: Geology, v. 23, p. 433–436.

Costa, F., Scaillet, B., and Pichavant, M., 2004, Petrological and experimental constraints on the preeruption conditions of Holocene dacite from Volcán San Pedro (36°S, Chilean Andes) and the importance of sulphur in silicic subduction-related magmas: Journal of Petrology, v. 45, p. 855–884.

Couch, S., Sparks, R.S.J., and Carroll, M.R., 2001, Mineral disequilibrium in lavas explained by convective self-mixing in open magma chambers: Nature, v. 411, p. 1037–1039.

de Saint-Blanquat, M., Horsman, E., Habert, G., Morgan, S., Vanderhaeghe, O., Law, R., and Tikoff, B., 2011, Multiscale magmatic cyclicity, duration of pluton construction, and the paradoxical relationship between tectonism and plutonism in continental arcs: Tectonophysics, v. 500, p. 20–33.

Dilles, J.H., 1984, The petrology and geochemistry of the Yerington batholith and the Ann-Mason porphyry copper deposit, western Nevada: Ph.D. thesis, Stanford, California, Stanford University, 389 p.

Dilles, J.H.,1987, Petrology of the Yerington batholith, Nevada; evidence for evolution of porphyry copper ore fluids: Economic Geology, v. 82, p. 1750–1789.

Dilles, J.H., 2000, Cupolas and convection in crystallizing granitoids as a means of extracting aqueous fluids to produce porphyry Cu-Mo-Au deposits: Geological Society of America, Annual Meeting, 112th, Reno, Nevada, November

9–18, 2000, Abstracts, v. 32, p. A-51.

Dilles, J.H., and Einaudi, M.T., 1992, Wall rock alteration and hydrothermal flow paths about the

Ann-Mason porphyry copper deposit, Nevada; a 6-km vertical reconstruction: Economic Geology, v. 87, p. 1963–2001.

Dilles, J.H., and Proffett, J.M., 1995, Metallogenesis of the Yerington batholith, Nevada, *in* Pierce, F.W., and Bolm, J.G., eds., Porphyry copper deposits of the American cordillera: Arizona Geological Society Digest, v. 20, p. 306–315.

Dilles, J.H., and Wright, J.E., 1988, The chronology of early Mesozoic arc magmatism in the Yerington district of western Nevada and its regional implications: Geological Society of America Bulletin, v. 100, p. 644–652.

Dilles, J.H., Proffett, J., and Einaudi, M.T., 2000, Magmatic and hydrothermal features of the Yerington batholith with emphasis on the porphyry Cu(Mo) deposit in the Ann-Mason area: Society of Economic Geologists Guidebook, v. 32, p. 67–90.

Dilles, J.H., Kent, A.J.R., Wooden, J.L., Tosdal, R.M., Koleszar, A., Lee, R.G., and Farmer, L.P., 2015, Zircon compositional evidence for sulfur-degassing from ore-forming arc magmas: Economic Geology, v. 110, p. 241–251.

Eggler, D.H., 1972, Water-saturated and undersaturated melting relations in a Paricutin andesite and an estimate of water content in the natural magma: Contributions to Mineralogy and Petrology, v. 34, p. 261–271.

Einaudi, M.T., 2000, Skarns of the Yerington district, Nevada: A triplog and commentary: Society of Economic Geologists Guidebook, v. 32, p. 101–126.

Fournier, R.O., 1999, Hydrothermal processes related to movement of fluid from plastic into brittle rock in the magmatic-epithermal environment: Economic Geology, v. 94, p. 1193–1211.

Gilmer, A., Sparks, R.S.J., Rust, A.C., Tapster, S., Webb, A.D., and Barfod, D.N., 2017, Geology of the Don Manuel igneous complex, central Chile: Implications for igneous processes in porphyry copper systems: Geological Society of America Bulletin, v. 129, doi: 10.1130/B31524.1.

Glazner, A.F., Bartley, J.M., Coleman, D.S., Gray, W., and Taylor, R.Z., 2004, Are plutons assembled over millions of years by amalgamation from small magma chambers?: GSA Today, v. 14, p. 4–12.

Harrison, M.T., Grove, M., McKeegan, K.D., Coath, C.D., Lovera, O.M., and Le Fort, P., 1999, Origin and episodic emplacement of the Manaslu intrusive complex, central Himalaya: Journal of Petrology, v. 40, p. 3–19.

Hayba, D.O., and Ingebritsen, S.E., 1997, Multiphase groundwater flow near cooling plutons: Journal of Geophysical Research, v. 102, p. 12,235–12,252.

Huber, C., Bachmann, O., and Manga, M., 2009, Homogenization processes in silicic magma chambers by stirring and mushification (latent heat buffering): Earth and Planetary Science Letters, v. 283, p. 38–47.

Huber, C., Bachmann, O., and Dufek, J., 2010, The limitations of melting on the reactivation of silicic mushes: Journal of Volcanology and Geothermal Research, v. 195, p. 97–105.

Ingebritsen, S.E., 2012, Modeling the formation of porphyry copper deposits: Science, v. 338, p. 1551–1552.

Ingebritsen, S.E., and Appold, M., 2012, The physical hydrogeology of ore deposits: Economic Geology, v. 107, p. 559–584.

Lipske, J.L., and Dilles, J.H., 2000, Advanced argillic and sericitic alteration in the subvolcanic environment of the Yerington porphyry copper system, Buckskin Range, Nevada: Society of Economic Geologists Guidebook, v. 32, p. 91–100.

Longo, A.A., Dilles, J.H., Grunder, A.L., and Duncan, R., 2010, Evolution of calc-alkaline volcanism and associated hydrothermal gold deposits at Yanacocha, Perú: Economic Geology, v. 105, p. 1191–1241, plus geology map plate.

Loucks, R.R., 2014, Distinctive composition of copper-ore-forming arc magmas: Australian Journal of Earth Sciences, v. 61, p. 5–16.

Matzel, J.E.P., Bowring, S.A., and Miller, R.B., 2006, Time scales of pluton construction at differing crustal levels: Examples from the Mount Stuart and Tenpeak intrusions, North Cascades, Washington: Geological Society of America Bulletin, v. 118, p. 1412–1430.

Menand, T., Annen, C., and de Saint-Blanquat, M., 2015, Rates of magma transfer in the crust: Insights into magma reservoir recharge and pluton growth: Geology, v. 43, p. 199–202.

Michaut, C., and Jaupart, C., 2006, Ultra-rapid formation of large volumes of evolved magma: Earth and Planetary Science Letters, v. 250, p. 38–52.

Michel, J., Baumgartner, L., Putlitz, B., Schaltegger, U., and Ovtcharova, M., 2008, Incremental growth of the Patagonian Torres del Paine laccolith over 90 k.y.: Geology, v. 36, p. 459–462.

Morgan, S., Stanik, A., Horsman, E., Tikoff, B., de Saint Blanquat, M., and Habert, G., 2008, Emplacement of multiple magma sheets and wall rock deformation: Trachyte Mesa intrusion, Henry Mountains, Utah: Journal of Structural Geology, v. 30, p. 491–512.

Naney, M.T., 1983, Phase equilibria of rock-forming ferromagnesian silicates in granitic systems: American Journal of Science, v. 283, p. 993–1033.

Newman, S., and Lowenstern, J.B., 2002, VolatileCalc: A silicate melt-H_2OCO_2 solution model written in Visual Basic for Excel: Computers and Geosciences, v. 28, p. 597–604.

Norton, D., and Knight, J.E., 1977, Transport phenomena in hydrothermal systems: Cooling plutons: American Journal of Science, v. 277, p. 937–981.

Petford, N.K., and Gallagher, K., 2001, Partial melting of mafic (amphibolitic) lower crust by periodic influx of basaltic magma: Earth Planetary Science Letters, v. 193, p. 483–489.

Piwinskii, A.J., and Wyllie, P., 1970, Experimental studies of igneous rock series: Felsic body suite from the Needle Point pluton, Wallowa batholith, Oregon: Journal of Geology, v. 78, p. 52–76.

Proffett, J.M., 2009, High Cu grades in porphyry Cu deposits and their relationship to

emplacement depth of magmatic sources: Geology, v. 37, p. 675–678.

Proffett, J.M., and Dilles, J.H., 1984, Geological map of the Yerington district, Nevada: Nevada Bureau of Mines and Geology, map 77, scale 1:24,000.

Scaillet, B., Holtz, F., and Pichavant, M., 2016, Experimental constraints on the formation of silicic magmas: Elements, v. 12, p. 109–114.

Schöpa, A., and Annen, C., 2013, The effects of magma flux variations on the formation and lifetime of large silicic magma chambers: Journal of Geophysical Research: Solid Earth, v. 118, p. 926–942.

Sillitoe, R.H., 2010, Porphyry copper systems: Economic Geology, v. 105, p. 3–41.

Sparks, R.S.J., 1978, The dynamics of bubble formation and growth in magmas: A review and analysis: Journal of Volcanology and Geothermal Research, v. 3, p. 1–37.

Sparks, R.S.J., Huppert, H.E., and Turner, J.S., 1984, The fluid dynamics of evolving magma chambers, *in* Moorbath, S., Thompson, R.N., and Oxburgh, E.R., eds., The relative contributions of mantle, oceanic crust and continental crust to magma genesis: Philosophical Transactions of the Royal Society of London, Series A: Mathematical and Physical Sciences, v. 310, p. 511–534.

Spencer, E.T., Wilkinson, J.J., Creaser, R.A., and Seguel, J., 2015, The distribution and timing of molybdenite mineralization at the El Teniente Cu-Mo porphyry deposit, Chile: Economic Geology, v. 110, p. 387–421.

Steinberger, I., Hinks, D., Driesner, T., and Heinrich, C.A., 2013, Source plutons driving porphyry copper ore formation: Combining geomagnetic data, thermal constraints, and chemical mass balance to quantify the magma chamber beneath the Bingham Canyon deposit: Economic Geology, v. 108, p. 605–624.

Tait, S., Jaupart, C., and Vergniolle, S., 1989, Pressure, gas content, and eruption periodicity of a shallow, crystallizing magma chamber: Earth and Planetary Science Letters, v. 92, p. 107–123.

Tapster, S., Condon, D., Naden, J., Noble, S., Petterson, M., Roberts, N., Saunders, A., and Smith, D., 2016, Rapid thermal rejuvenation of high-crystallinity magma linked to porphyry copper deposit formation; evidence from the Koloula porphyry prospect, Solomon Islands: Earth and Planetary Science Letters, v. 442, p. 206–217.

Wessel, P., Smith, W.H.F., Scharroo, R., Luis, J., Wobbe, F., 2013, Generic mapping tools: Improved version released: Eos, Transactions American Geophysical Union, v. 94, p. 409–410.

White, S.M., Crisp, J.A., and Spera, F.J., 2006, Long-term volumetric eruption rates and magma budgets: Geochemistry, Geophysics, Geosystems, v. 7, doi: 10.1029/2005GC001002.

Whittington, A., Hofmeister, A., Nabelek, P., 2009, Temperature-dependent thermal diffusivity of the Earth's crust and implications for magmatism: Nature, v. 458, p. 319–321.

von Quadt, A., Erni, M., Martinek, K., Moll, M., Peytcheva, I., and Heinrich, C.A., 2011, Zircon crystallization and the lifetimes of ore-forming magmatic-hydrothermal systems: Geology, v. 39, p. 731–734.
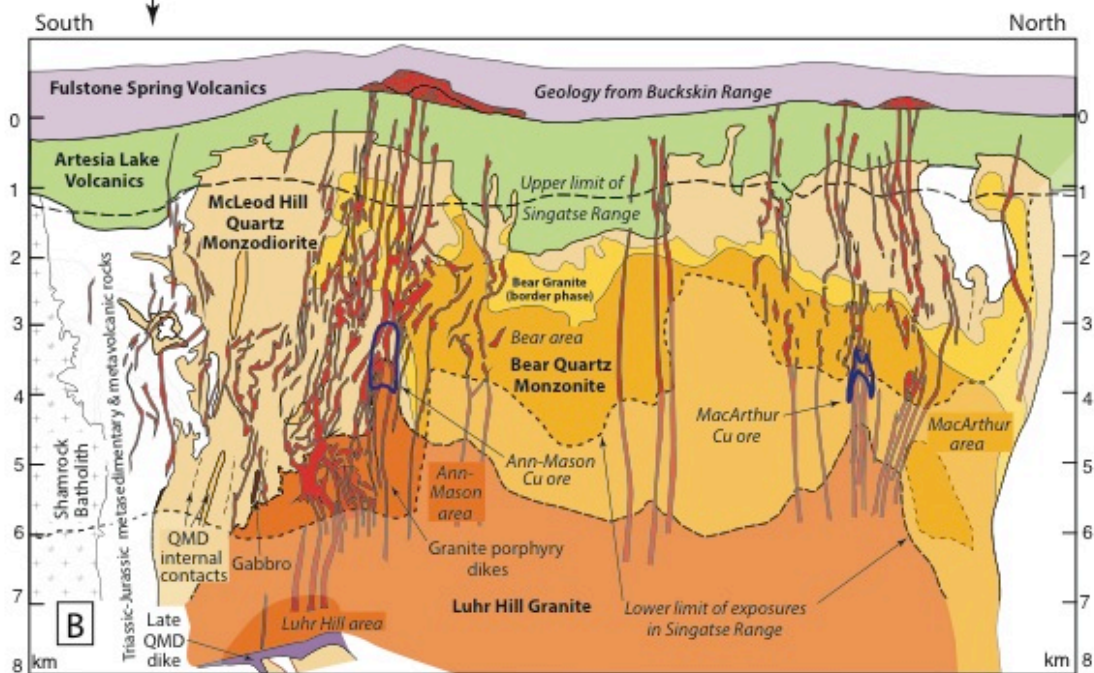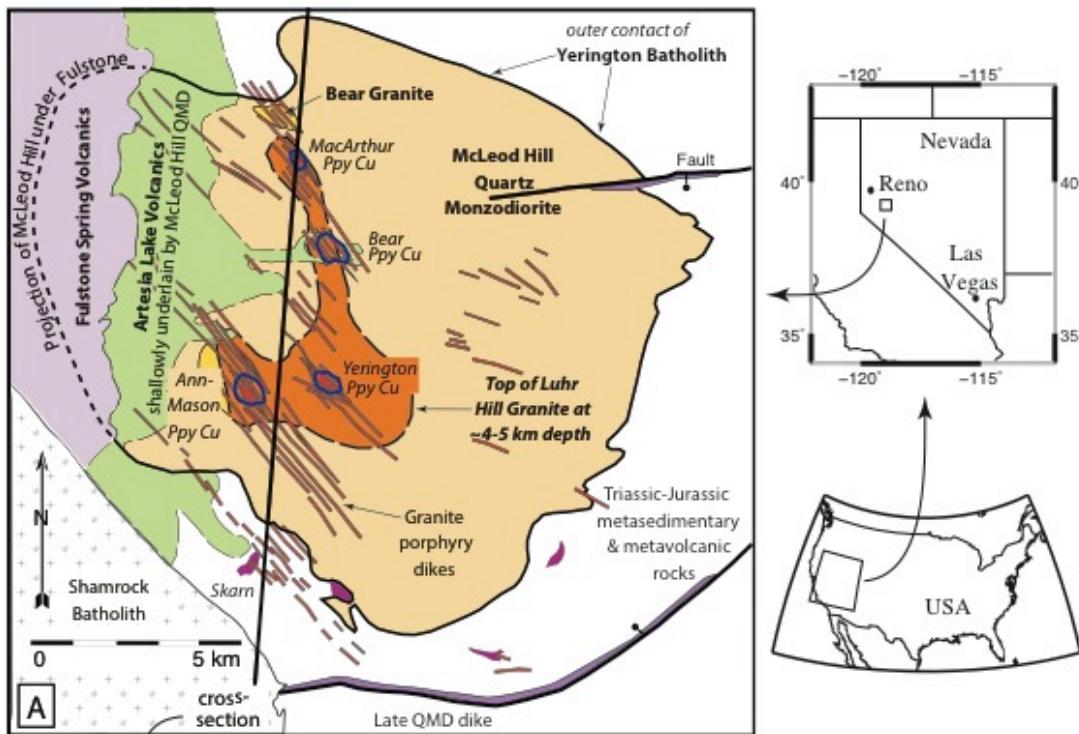
A

outer contact of
Yerington Batholith

Projection of McLeod Hill under Fulstone

Fulstone Spring Volcanics

Bear Granite

MacArthur Ppy Cu

McLeod Hill Quartz Monzodiorite

Fault

Artesia Lake Volcanics shallowly underlain by McLeod Hill QMD

Bear Ppy Cu

Ann-Mason Ppy Cu

Yerington Ppy Cu

Top of Luhr Hill Granite at ~4-5 km depth

N

Shamrock Batholith

Granite porphyry dikes

Triassic-Jurassic metasedimentary & metavolcanic rocks

0   5 km

Skarn

cross-section

Late QMD dike

−120°   −115°

Nevada

40°   40°

● Reno

Las Vegas

35°   35°

−120°   −115°

USA

B

South   North

Fulstone Spring Volcanics   *Geology from Buckskin Range*

0   0

Artesia Lake Volcanics

1   *Upper limit of Singatse Range*   1

McLeod Hill Quartz Monzodiorite

2   **Bear Granite (border phase)**   2

3   *Bear area*   3

Bear Quartz Monzonite

4   *MacArthur Cu ore*   *MacArthur area*   4

Ann-Mason Cu ore

5   *Ann-Mason area*   5

6   *Lower limit of exposures in Singatse Range*   6

QMD internal contacts   Gabbro   Granite porphyry dikes

7   **Luhr Hill Granite**   7

Late QMD dike   *Luhr Hill area*

8 km   8 km

Shamrock Batholith

Triassic-Jurassic metasedimentary & metavolcanic rocks

Fig. 1. (A) Reconstructed plan map of the Yerington batholith as exposed below the Cenozoic unconformity at 0- to 2-km original depth after Proffett (2009) and Dilles and Proffett (1995). (B) North-south (pretilt) cross section of the Yerington batholith based on mapped exposures in the Singatse Range, showing projected geology from the Buckskin Range on the west and the Luhr Hill area on the east. The early McLeod Hill quartz monzodiorite (QMD) is a polyphase intrusion associated with small bodies of cumulate gabbro and was intruded by the Bear quartz monzonite and its upper granite border phase. The deep Luhr Hill granite is the source of porphyry dikes associated with skarn and porphyry copper mineralization (Ppy Cu). Modified from Proffett and Dilles (1984) and Dilles (1987).
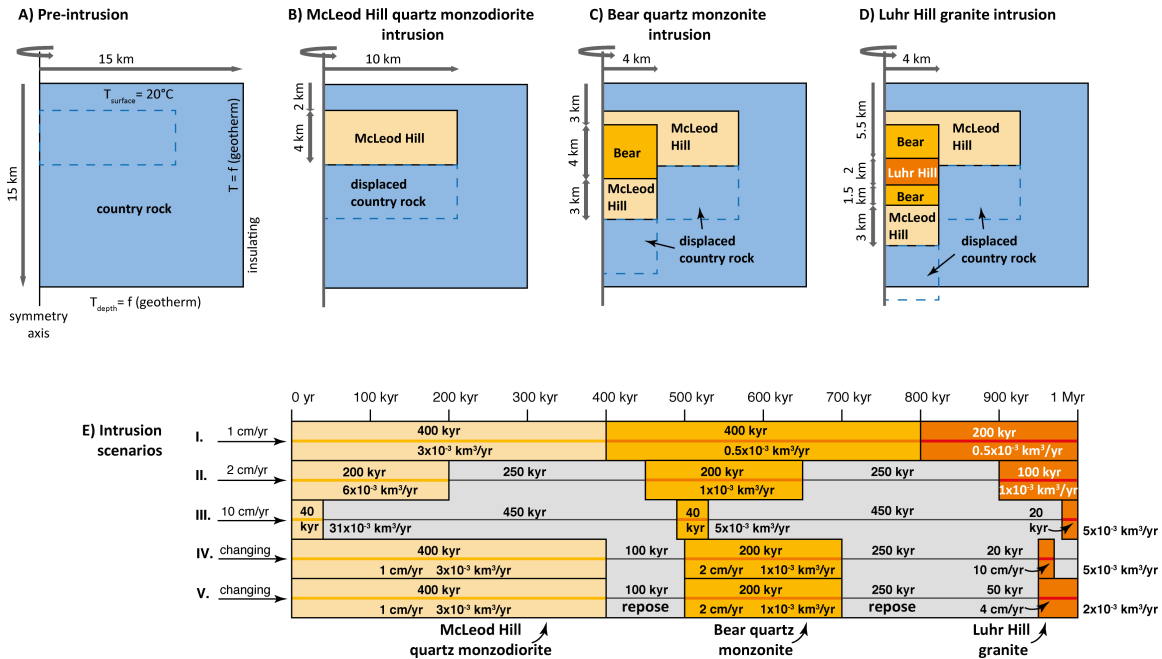
Fig. 2. Timelines and geometry of the Yerington batholith used in the numerical model (see also Table 1). Initial temperature conditions of the country rock are calculated based on the geothermal gradient. The surface of the modeling domain is at a constant temperature of 20°C; the right boundary is insulating and does not allow heat to flux through. The modeling domain is axisymmetric with the axis of symmetry on the left. (A) Initial conditions prior to magma emplacement. (B) Emplacement of the McLeod Hill quartz monzodiorite. The country rock is displaced downward. (C) Emplacement of the Bear quartz monzonite into the lower part of the McLeod Hill quartz monzodiorite. The latter is displaced downward. (D) Emplacement of the Luhr Hill into the lower part of the Bear quartz monzonite. We note that some parts of the country rock are displaced out of the bounds of the modeling domain. However, this is not important as we focus our analysis on the three intrusions of the Yerington batholith. (E) Timeline showing intrusive periods and repose periods for five scenarios (see also Table 2).
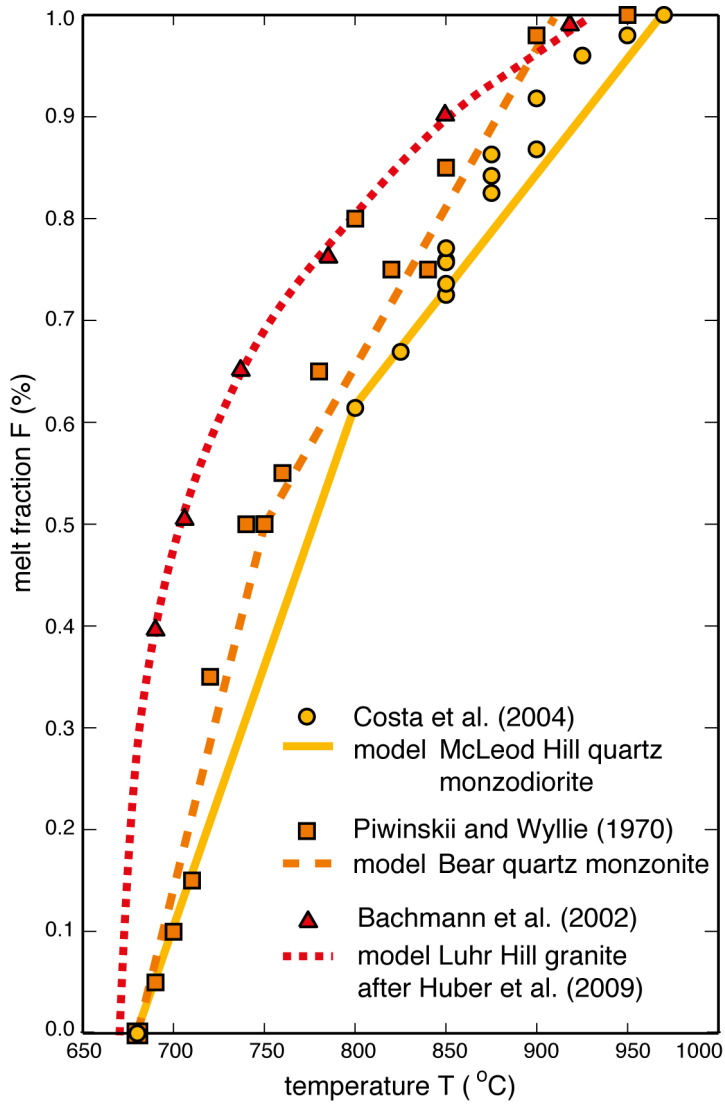
Fig. 3. Temperature-melt fraction (*T-F*) relationships for the melts used in the model (lines) in comparison to published experimental results (symbols) for bulk compositions comparable to the three principal Yerington magmas, McLeod Hill quartz monzodiorite (solid line), Bear quartz monzonite (dashed line), and Luhr Hill granite (dotted line).
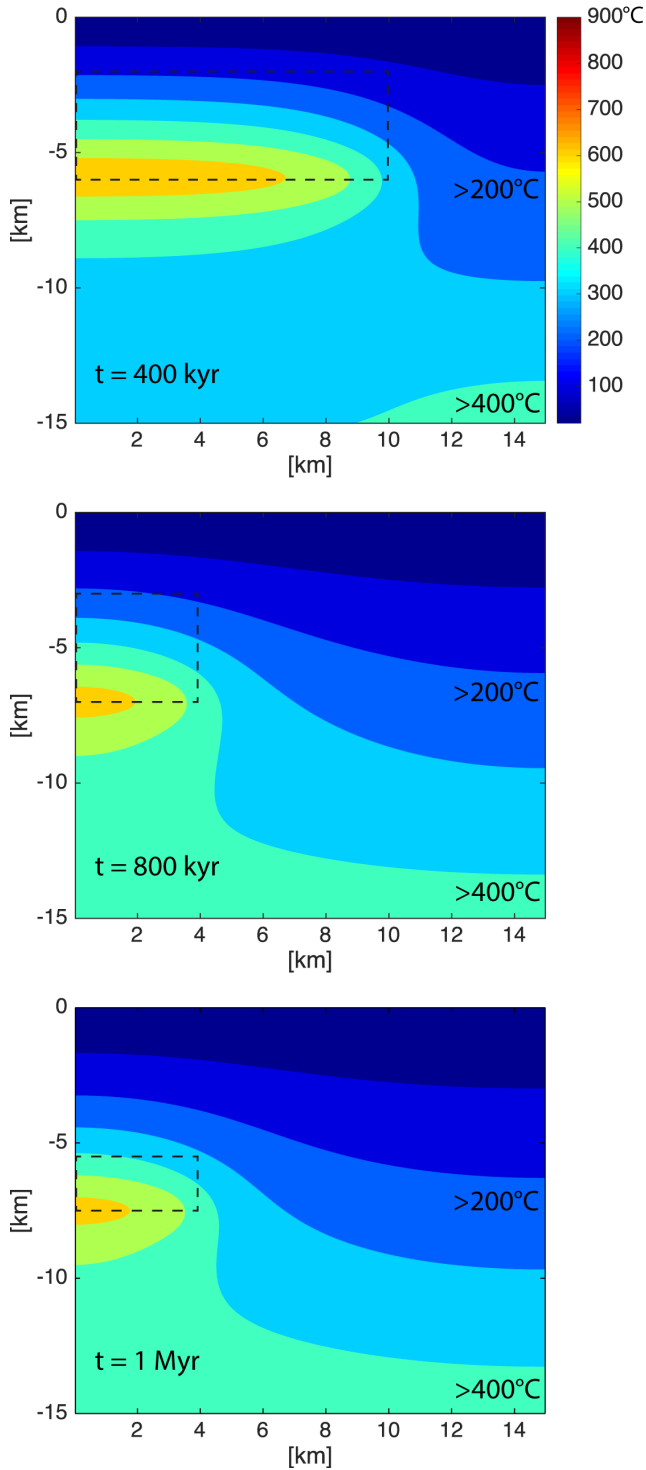
Fig. 4. Scenario I. Emplacement of the Yerington batholith at a steady rate of 1 cm/yr without repose period between the three units. Snapshots of temperatures are shown at the end of McLeod quartz monzodiorite intrusion (t = 400 k.y.), at the end of Bear quartz monzonite (t = 800 k.y.) and at the end of Luhr Hill granite (t = 1 m.y.). Each magma increment solidifies rapidly, and no melt persists in the system. Fillings correspond to temperature; dashed boxes show the outline of the three intrusions. The left side of the diagram is the symmetry axis of the system.
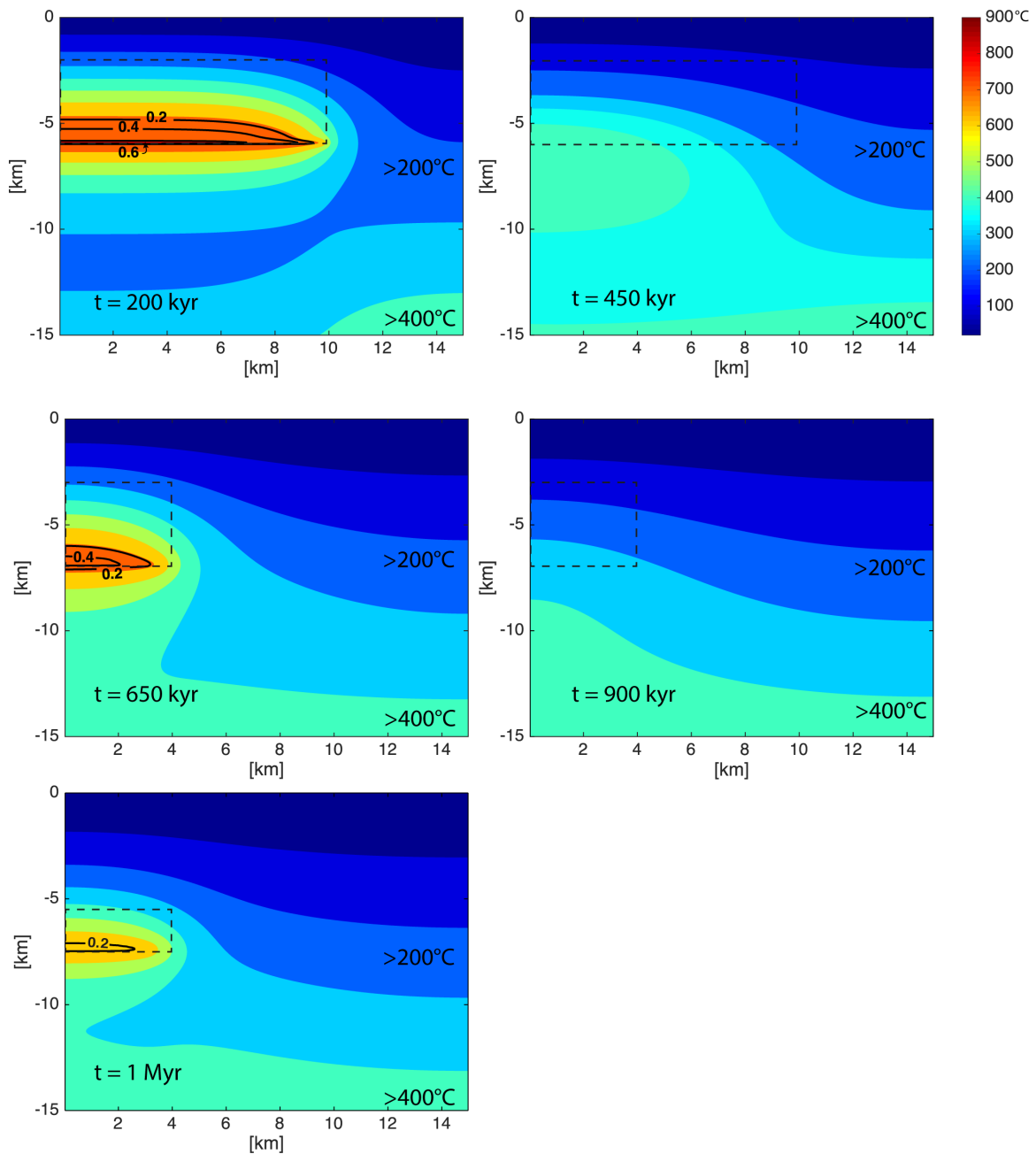
Fig. 5. Scenario II. Each unit is emplaced at a rate of 2 cm/yr. The repose period between units is 250 k.y. Snapshots of temperatures are shown when the amount of melt is maximum at the end of each unit emplacement, i.e., t = 200 k.y. for McLeod Hill quartz monzodiorite, t = 650 k.y. for Bear quartz monzonite, and t = 1 m.y. for Luhr Hill granite. Snapshots are also shown for the end of the repose periods (t = 450 k.y. and t = 900 k.y.). No melt is present at the end of the repose periods. Fillings correspond to temperature and contour lines to melt fractions; dashed boxes show the outline of the three intrusions.
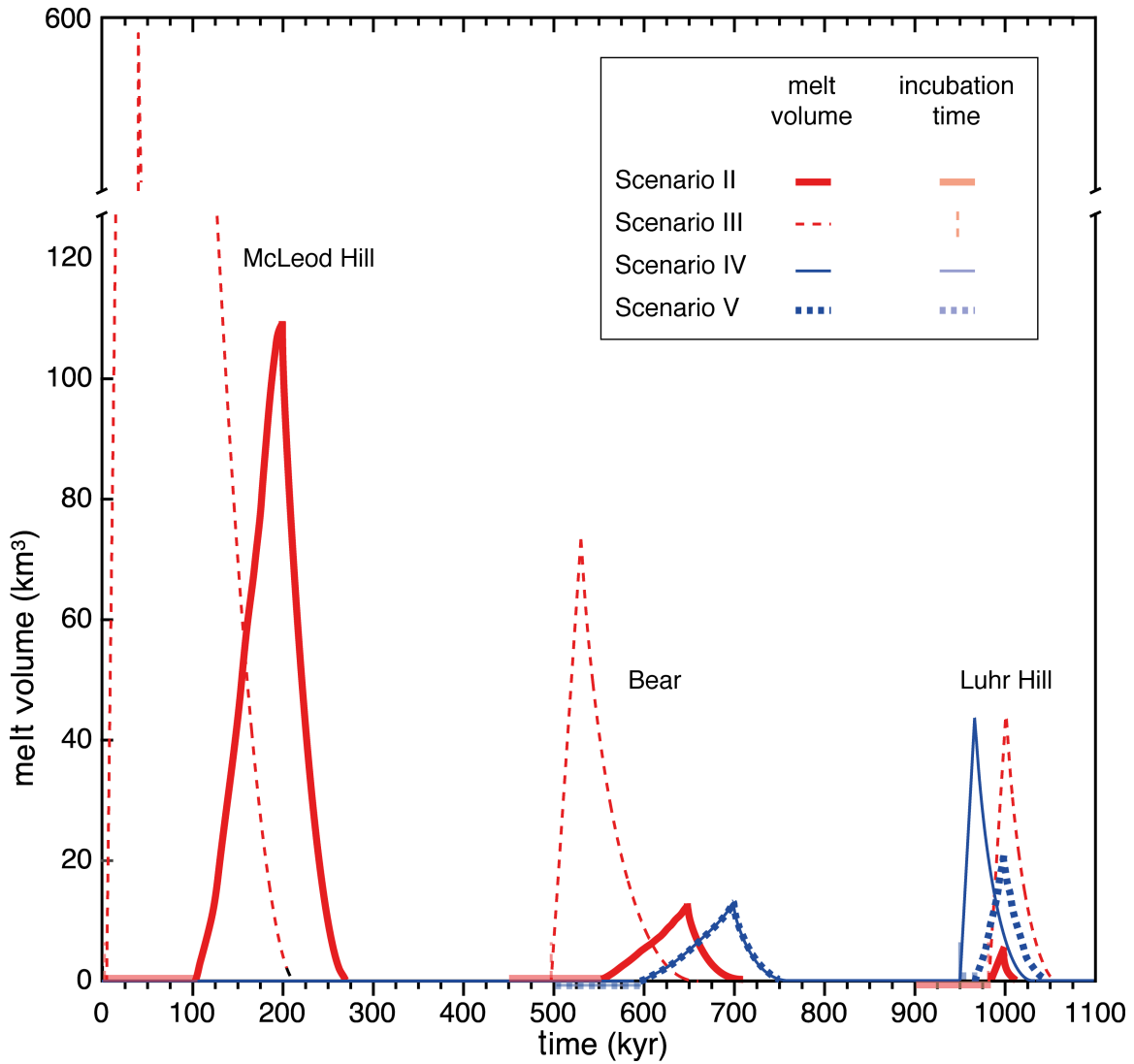
Fig. 6. Evolution of melt volumes over time for scenarios II–V (black lines). Horizontal gray lines at the x-axis show incubation times (the time span from the start of the magma emplacement to the point when permanent melt starts to accumulate; see also Table 2). The incubation times for scenario III and for the Luhr Hill granite in scenario IV are very short and indicated by vertical gray lines. The melt volume and the incubation time curves for scenarios IV and V superpose for Bear quartz monzonite. Maximum melt volumes accumulate at the end of the intrusion emplacement times.
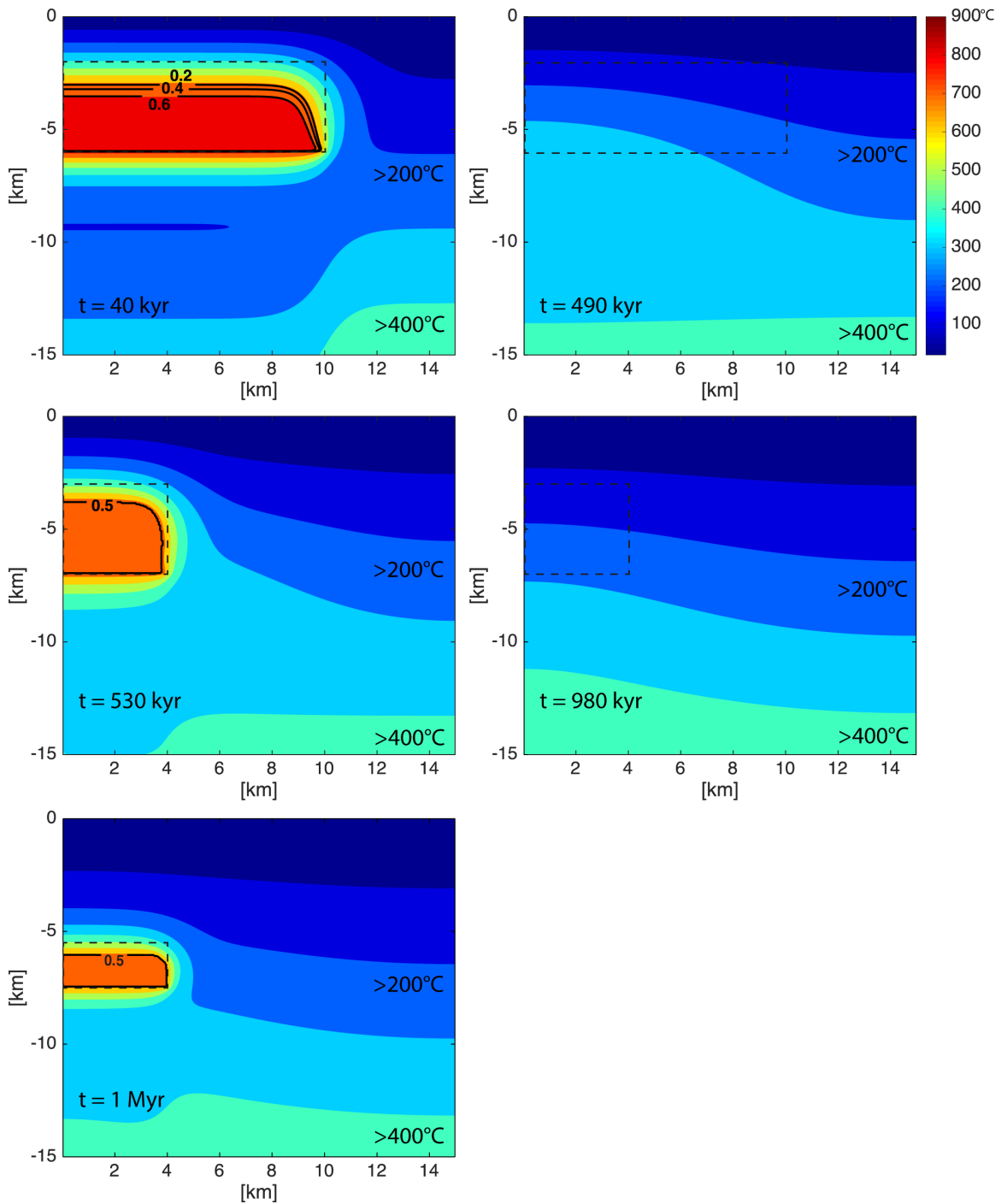
Fig. 7. Scenario III. Each unit is emplaced at a rate of 10 cm/yr. The repose period between units is 450 k.y. Snapshots of temperatures are shown when the amount of melt is maximum at the end of each unit emplacement, i.e., t = 40 k.y. for McLeod Hill quartz monzodiorite, t = 530 k.y. for Bear quartz monzonite, and t = 1 m.y. for Luhr Hill granite. Snapshots are also shown for the end of the repose periods (t = 490 k.y. and t = 980 k.y.). No melt is present at the end of the repose periods. Fillings correspond to temperature and contour lines to melt fractions; dashed boxes show the outline of the three intrusions.
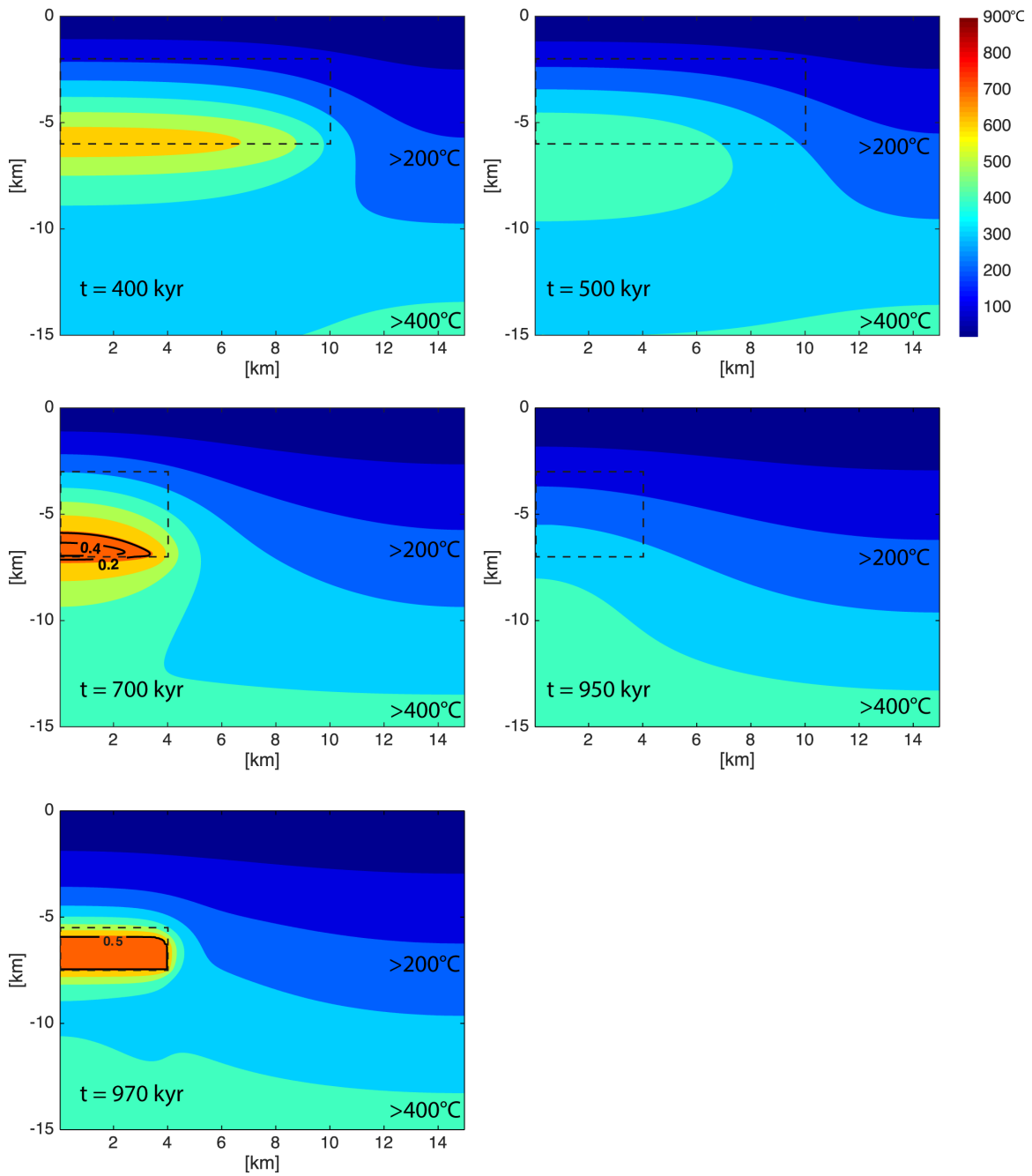
Fig. 8. Snapshots of temperatures and melts for scenario IV. The emplacement rate of McLeod Hill quartz monzodiorite is 10 cm/yr and is followed by a 100-k.y. repose period; the emplacement rate of Bear quartz monzonite is 2 cm/yr and is followed by a repose period of 250 k.y.; the emplacement rate of Luhr Hill granite is 10 cm/yr. Snapshots of temperatures are shown when the amount of melt is maximum at the end of each unit emplacement, i.e., at t = 400 k.y., t = 700 k.y., and t = 970 k.y., and at the end of repose periods at t = 500 k.y. and t = 950 k.y. No melt is present at the end of the repose periods. Fillings correspond to temperature and contour lines to melt fractions; dashed boxes show the outline of the three intrusions.
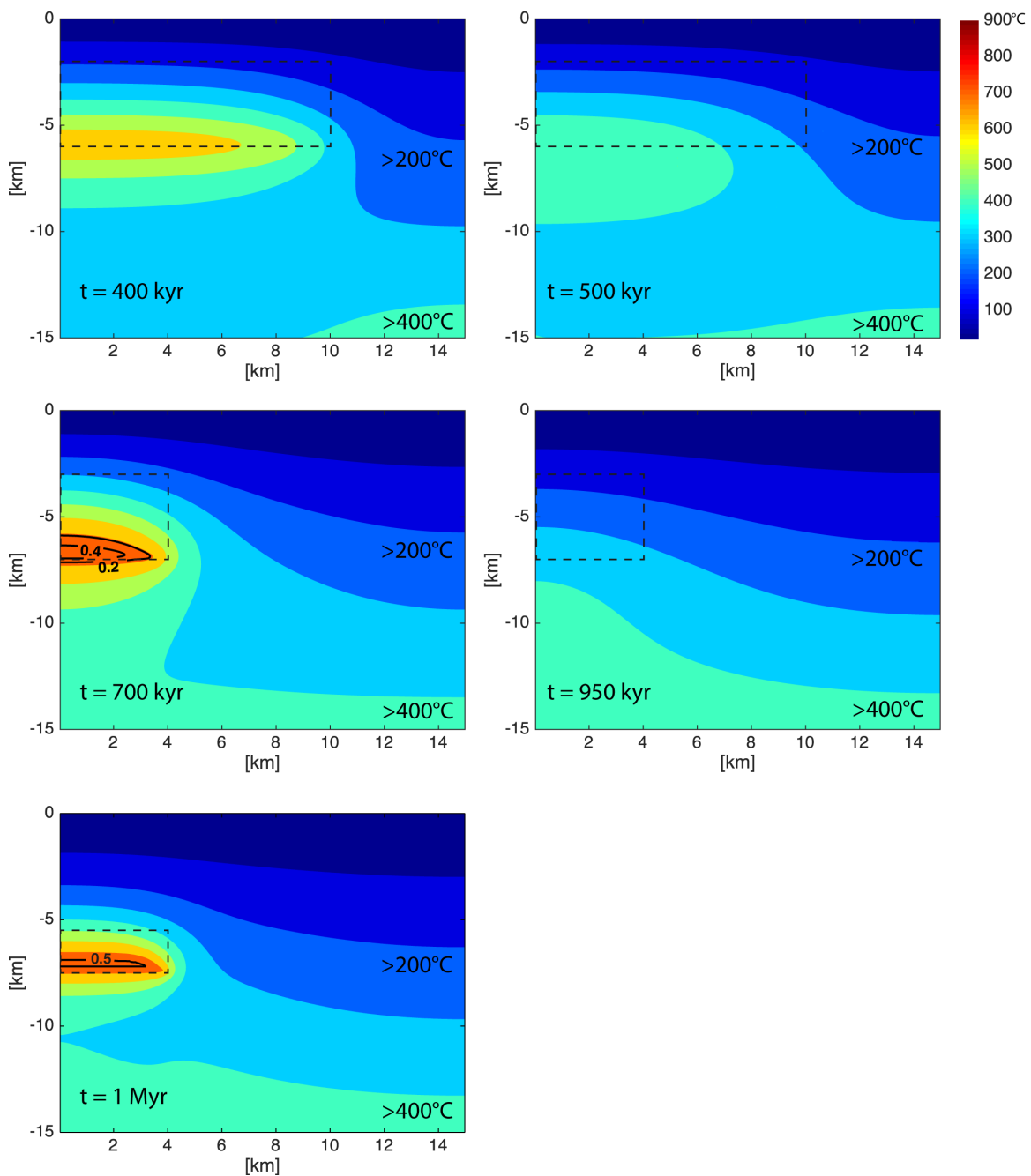
Fig. 9. Snapshots of temperatures and melts for scenario V. The emplacement rate of McLeod Hill quartz monzodiorite is 10 cm/yr and is followed by a 100-k.y. repose period; the emplacement rate of Bear quartz monzonite is 2 cm/yr and is followed by a repose period of 250 k.y.; the emplacement rate of Luhr Hill granite is 4 cm/yr. Snapshots of temperatures are shown when the amount of melt is maximum at the end of each unit emplacement, i.e., at t = 400 k.y., t = 700 k.y., and t = 1 m.y., and at the end of repose periods at t = 500 k.y. and t = 950 k.y. No melt is present at the end of the repose periods. Fillings correspond to temperature and contour lines to melt fractions; dashed boxes show the outline of the three intrusions.
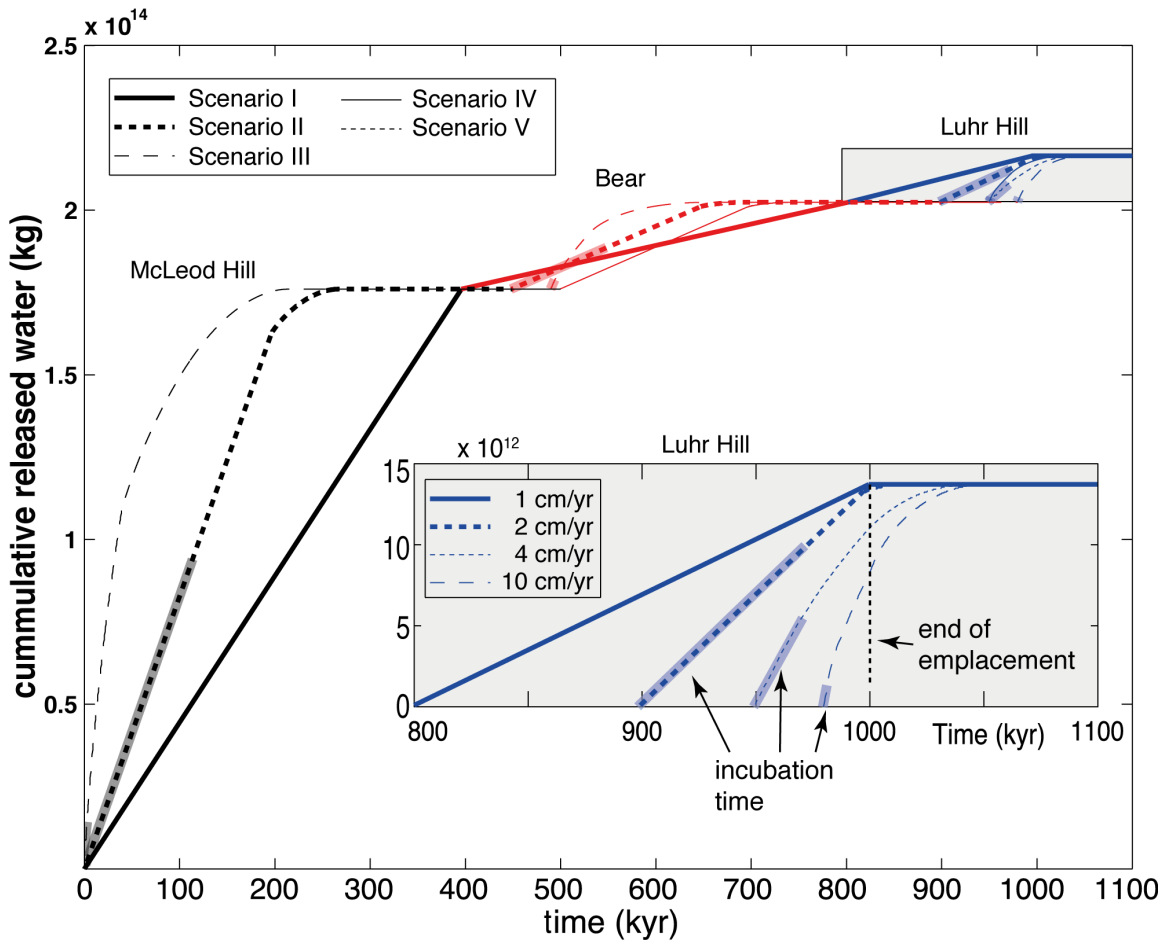
Fig. 10. Cumulative mass of water released by decompression and magma crystallization over time for the different scenarios. The water content of the magma is determined by the magma temperature, melt fraction, and the water saturation value at emplacement depth (eq. 2). Volatiles are released after the end of a unit emplacement only when the emplacement rate was fast enough for significant amounts of melt to accumulate. Plateaus in the curve correspond to the absence of melt during repose periods. The curves for scenarios I, IV, and V superpose for McLeod Hill quartz monzodiorite, and the curves for scenarios IV and V superpose for Bear quartz monzonite. Thick gray lines show incubation times from the start of unit emplacement to the point when melt starts to accumulate. Inset displays the cumulated mass of water released for the Luhr Hill granite at different emplacement rates (without scenario IV, as the emplacement rate is the same as for scenario III).
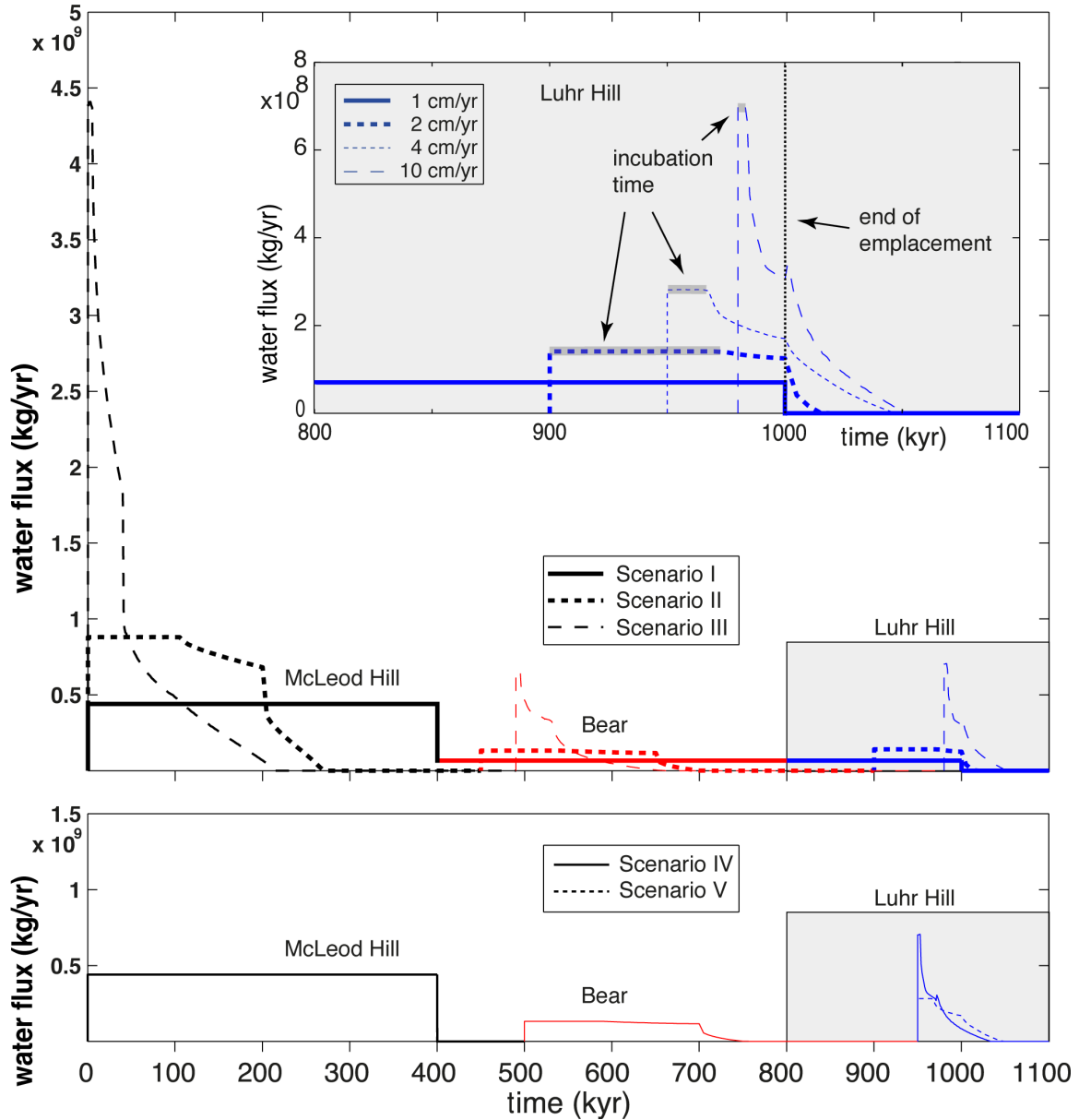
Fig. 11. Water fluxes over time for the different scenarios. Inset displays the water flux for the Luhr Hill granite at different emplacement rates (without scenario IV, as the emplacement rate is the same as for scenario III). Thick gray lines show incubation times from the start of unit emplacement to the point when melt starts to accumulate; dotted line shows the end of magma emplacement.
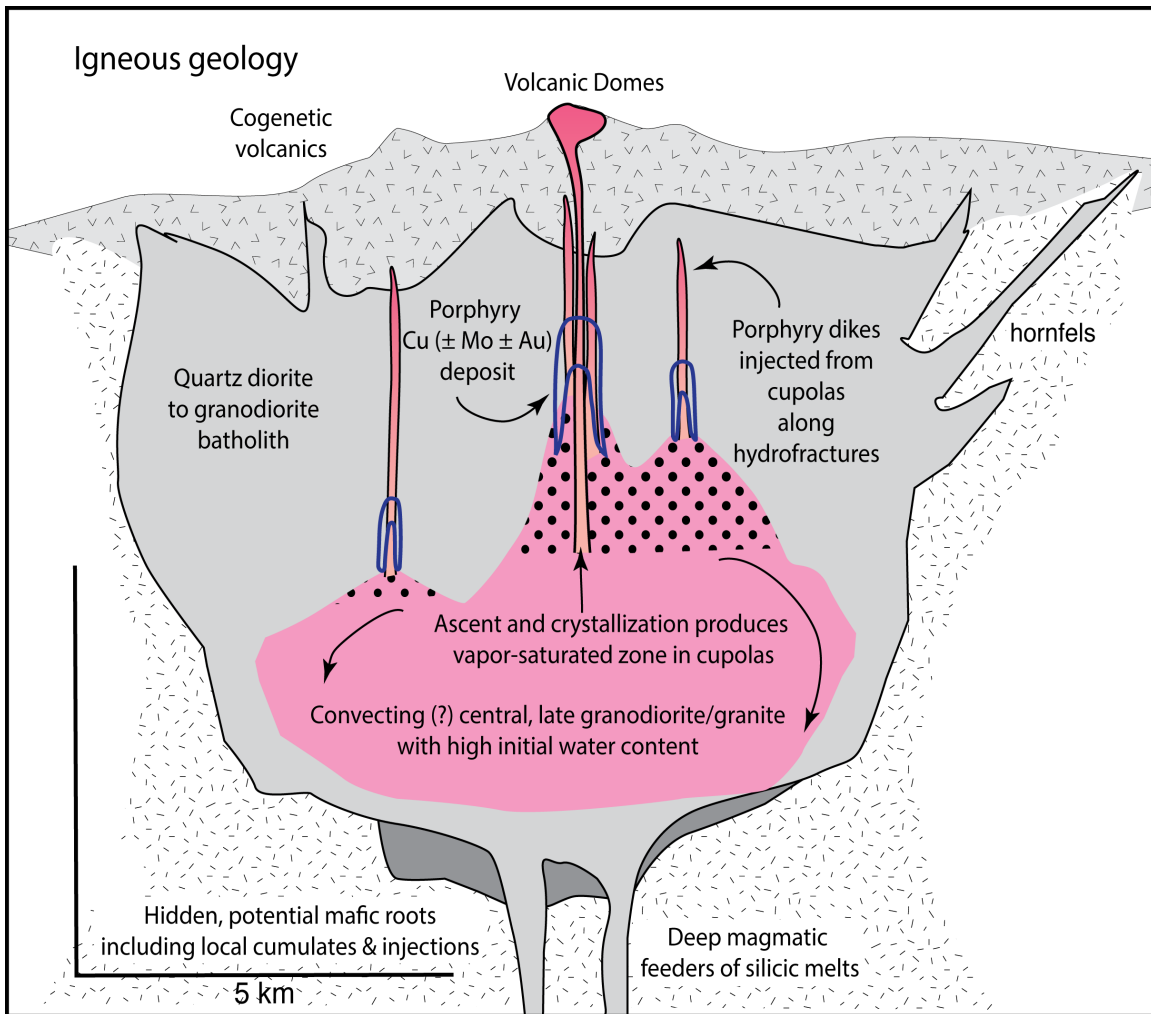
Fig. 12. Cross-section cartoon based on the Yerington batholith and similar magmatic-hydrothermal systems. Igneous rocks and geology illustrating positions of porphyry Cu (±Mo±Au) ores with respect to cupola sources of magmatic-hydrothermal fluids and porphyry dikes. For the Yerington batholith, the early McLeod Hill quartz monzodiorite and Bear quartz monzonite units are not differentiated, and the Luhr Hill granite is the source of porphyry dikes.

the Numerical Model

	Volume (km^3)	Radius (km)	Depth (km)	$T_{solidus}$ (°C)	$T_{liquidus}$ (°C)	$T_{emplacement}$ (°C)	Melt fraction at $T_{emplacement}$ (%)	Water content (wt-%)	Conductivity (W m^{-1} K^{-1})	Density (kg m^{-3})	Specific heat capacity (J kg^{-1} K^{-1})	Latent heat (J kg^{-1})
odiorite	1257	10	2-6	680	970	920	0.9	6	2.5	2700	1000	3.5×10^5
	201	4	3-7	680	910	850	0.8	6	2.5	2700	1000	3.5×10^5
	100	4	5.5-7.5	675	925	850	0.9	6	2.5	2700	1000	3.5×10^5

TABLE 2. Parameters for the Numerical Simulations and Computed Time Scales

Intrusion Name	Volume (km^3)	Emplacement duration (kyr)	Emplacement rate (cm/yr)	Volumetric emplacement rate (km^3/yr)	Incubation time (kyr)	Post-intrusion cooling time (kyr)
McLeod Hill quartz monzodiorite	1257	400	1	3 x 10^{-3}	no melt	no melt
		200	2	6 x 10^{-3}	105	72
		40	10	31 x 10^{-3}	5	174
Bear quartz monzonite	201	400	1	0.5 x 10^{-3}	no melt	no melt
		200	2	1 x 10^{-3}	90	59
		40	10	5 x 10^{-3}	5	140
Luhr Hill granite	100	200	1	0.5 x 10^{-3}	no melt	no melt
		100	2	1 x 10^{-3}	70	12
		50	4	2 x 10^{-3}	15	46
		20	10	5 x 10^{-3}	4	63